THESIS APPROVAL

GRADUATE SCHOOL, KASETSART UNIVERSITY

Master of Science (Chemistry)
DEGREE

Chemistry
FIELD

Chemistry
DEPARTMENT

TITLE: Structural Characteristics and Gas-sensing Properties of Sr(II) and Co(II) Doped $LaFeO_3$ Perovskites Prepared by Thermal Decomposition of Metal-organic Complexes

NAME: Mr. Thammanoon Thaweechai

THIS THESIS HAS BEEN ACCEPTED BY

THESIS ADVISOR
(Assistant Professor Nattamon Koonsaeng, Ph.D.)

THESIS CO-ADVISOR
(Assistant Professor Apirat Laobuthee, Ph.D.)

THESIS CO-ADVISOR
(Mr. Anurat Wisitsoraat, Ph.D.)

DEPARTMENT HEAD
(Assistant Professor Noojaree Prasitpan, Ph.D.)

APPROVED BY THE GRADUATE SCHOOL ON

DEAN
(Associate Professor Gunjana Theeragool, D.Agr.)

THESIS

STRUCTURAL CHARACTERISTICS AND GAS-SENSING PROPERTIES OF Sr(II) AND Co(II) DOPED $LaFeO_3$ PEROVSKITES PREPARED BY THERMAL DECOMPOSITION OF METAL-ORGANIC COMPLEXES

THAMMANOON THAWEECHAI

A Thesis Submitted in Partial Fulfillment of
The Requirements for the Degree of
Master of Science (Chemistry)
Graduate School, Kasetsart University
2010

Thammanoon Thaweechai 2010: Structural Characteristics and Gas-sensing Properties of Sr(II) and Co(II) Doped $LaFeO_3$ Perovskites Prepared by Thermal Decomposition of Metal-organic Complexes. Master of Science (Chemistry), Major Field: Chemistry, Department of Chemistry. Thesis Advisor: Assistant Professor Nattamon Koonsaeng, Ph.D. 101 pages.

Sr(II) and Co(II) doped $LaFeO_3$ perovskite compounds were successfully prepared by the thermal decomposition of metal-organic complexes which were synthesized from the reaction of $La(NO_3)_3.6H_2O$, $Fe(NO_3)_3.9H_2O$ and $N(CH_2CH_2OH)_3$ at 190 ºC in ethylene glycol solvent. Strontium nitrate and Cobalt chloride used as a dopant were varied in amounts as 0, 10.0, 30.0 and 50.0 mol%. The perovskite powders obtained by calcination of metal-organic complexes at 850 ºC for 4 h were characterized by FTIR, XRD, SEM and BET. The results from all characterizations exhibited that all of prepared perovskite powders were orthorhombic structure of $LaFeO_3$ phase with the crystallite sizes around 14.31-41.71 nm. The powders consisted of the agglomeration of very small, fine particles with the average secondary aggregated particle size of about 2-5 µm and the specific surface area around 7.88-18.99 m^2/g.

Based on semiconducting properties, the Sr(II) and Co(II) doped $LaFeO_3$ films prepared by spin coating were investigated for gas sensing. The results showed that all of prepared perovskites were p-type semiconductors. The doping of Sr(II) and Co(II) ions could improve the conductivity, sensitivity and selectivity of prepared sensors. The sensors doped with 50% Sr(II) exhibited the highest sensitivity to ethanol gas in the concentration range of 100-500 ppm at 350 ºC while the 10% doped Co(II) sensor showed the best response to 200-2000 ppm of acetone gas with high selectivity when compared to ethanol, methane and hydrogen gas.

______________________ ______________________ ___ / ___ / ___

Student's signature Thesis Advisor's signature

ACKNOWLEDGEMENTS

I would like to express by appreciation to my advisor, Assistant Professor Dr. Nattamon Koonsaeng, who has gave me worthy, helpful advices and encouraged me in my study and research. I am also especially grateful to my advisory committee Assistant Professor Dr. Apirat Laobuthee for many valuable suggestions and Dr. Anurat Wisitsoraat for his highly professional advices in gas-sensing study.

I would like to thank all of staffs at Department of Chemistry, Faculty of Science, Kasetsart University and Nanoelectronics and MEMS laboratory, Electronics and Computer Technology Center (NECTEC) for their kind helps and suggestions in everything that they can.

In addition, I would especially express my thanks to Thailand Graduate Institute of Science and Technology (TGIST) for grant that supported my study and research. I would also like to thank the Nanoelectronics and MEMS laboratory, Electronics and Computer Technology Center (NECTEC), Department of Materials and Engineering, Faculty of Engineering as well as Department of Chemistry, Faculty of Science, Kasetsart University for research facilities.

Finally, I would like to thank all of my friends who have helped me in a multitude of ways. I am also especially grateful to my family for their advices, encouragement and unflagging supports, without whose helps my study cannot has been succeeded.

Thammanoon Thaweechai
March, 2010

TABLE OF CONTENTS

Page

LIST OF TABLES

Table **Page**

LIST OF TABLES (Continued)

Table **Page**

Appendix Table

LIST OF TABLES (Continued)

LIST OF FIGURES

Figure **Page**

LIST OF FIGURES (Continued)

Appendix Figure

LIST OF FIGURES (Continued)

LIST OF ABBREVIATIONS

TEA = Triethanolamine
TGA = Thermal Gravimatric Analysis
XRD = X-Ray Powder Diffraction
JCPDS = Joint Committee on Powder Diffraction Standards
FTIR = Fourier Transform Infrared Spectroscopy
SEM = Scanning Electron Microscopy
BET = Brunauer, Emmett and Teller
EDS = Energy Dispersive X-Ray Spectroscopy
OM = Optical microscopy
LFO = $LaFeO_3$
LSFO10 = 10% Sr(II) doped $LaFeO_3$
LSFO30 = 30% Sr(II) doped $LaFeO_3$
LSFO50 = 50% Sr(II) doped $LaFeO_3$
LFCO10 = 10% Co(II) doped $LaFeO_3$
LFCO30 = 30% Co(II) doped $LaFeO_3$
LFCO50 = 50% Co(II) doped $LaFeO_3$

STRUCTURAL CHARACTERISTICS AND GAS-SENSING PROPERTIES OF Sr(II) AND Co(II) DOPED $LaFeO_3$ PEROVSKITES PREPARED BY THERMAL DECOMPOSITION OF METAL-ORGANIC COMPLEXES

INTRODUCTION

1. Lanthanum ferrite ($LaFeO_3$) compound

1.1 Structure of perovskite

The name perovskite was first called for minerals having a composition of $CaTiO_3$ in the 1893. It was discovered by the geologist Gustav Rose, who named it after the Russian mineralogist Count Lev Aleksevich von Perovski (Tanaka and Misono, 2001). In general, perovskite compound is a mixed metal oxide with the general formula of ABO_3, where B is a small transition metal cation and A is a larger of s-, d- or f-block cation. The ideal perovskite structure is cubic with space group $Pm3m\text{-}O_h$ as shown in Figure 1. In this structure, A and O ions form a cubic closest packing, in which A occupies at the centre of the cube with coordination of 12 to O, while B is contained in the interstitial site of an octahedral of O. The oxidation stats of A and B may be +2, +3 or +4, but must be six in total.

In nature, cubic perovskites are usually rare because the perovskite oxide mostly exists in the distorted structure. The deviation from the cubic structure can be measure by a tolerance factor (t) defined by Goldschmidt as given in the equation (1) (Pena and Fierro, 2001):

$$t = \frac{(r_A + r_O)}{\sqrt{2}(r_B + r_O)} \qquad \text{------ (1)}$$

where t is a tolerance factor

r_A, r_B *and* r_O is the ionic radius of A, B and O ion, respectively

The value of t is close to 1 for an ideal perovskite structure which appears in a few cases at high temperature. For distorted perovskites, the structures are preserved when the t value is between 0.8 and 1, and can be stable in orthorhombic, rhombohedral, tetragonal, monoclinic or triclinic system depended on cation type and temperature. The lanthanum ferrite used in this work is also stable in the orthorhombic structure at room temperature.

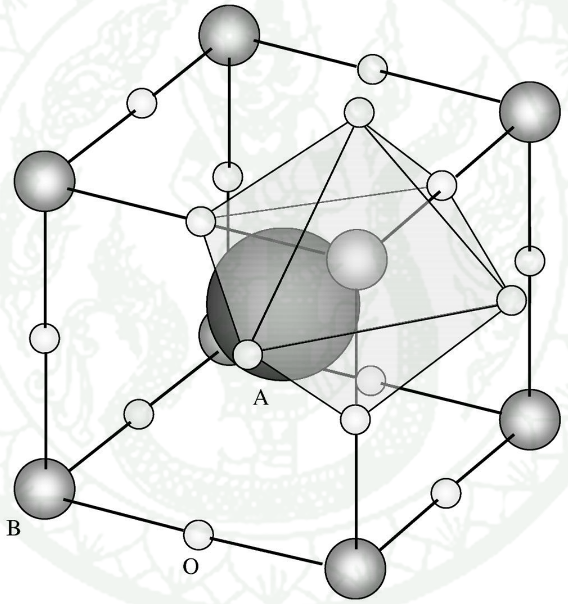

Figure 1 The ideal perovskite structure.

Source: Tanaka and Misono (2001)

1.2 Preparation method

It has been well known that the physical properties of metal oxide depend on preparation methods. Nowadays, there are many methods to synthesize perovskite oxides, and these methods have been extensively employed to produce perovskite and lanthanum ferrite compounds (Sunarso *at al.*, 2008):

1.2.1 Conventional powders methods

Conventional method is the most common preparing process to produce metal oxides from the reaction of mixed oxides, carbonates, hydroxides, or salts which are fired at temperature of at least two thirds of the melting point for periods above 10 hours. The size of prepared particles is controlled by mechanical mixing and grinding process of starting materials. The homogeneity and purity of the powders are considered poor because of the high temperature and the long reaction time. Many perovskite oxides have been prepared extensively using this process so-called solid state reaction (Li *et al*., 2002; Liou and Chen, 2008).

1.2.2 Co-precipitation

One of the oldest methods consisting of mixing an aqueous solution of metal ions with a precipitation agent followed by filtration, drying and thermal decomposition to obtain desired powders. The physical properties of powders are adjusted using pH, mixing rates, temperatures and concentrations of the reaction. The morphology, purity and composition control are considered good, and the particle size is in the range of few nanometers achieving by carful precipitation using suitable surfactants or capping agents. This technique is popular to synthesize $LaFeO_3$ although the different precipitation rates sometimes result in inhomogeneities products (Xiangfeng and Siciliano, 2003; Gosavi and Biniwale, 2010).

1.2.3 Sol-gel technique

Sol-gel technique involves about the production of a sol solution followed by dehydration at low temperature to acquire an amorphous-like gel. This technique delivers high purity and excellent composition control by applying different of modification routes such as alkoxide or alkoxide-salt route. However, many perovskite oxides including $LaFeO_3$ are largely synthesized using EDTA/citrate complexation route because of its advantages such as carbonate-free and chemically homogeneous in oxide products with a large surface area (Song *et al*., 2005; Shabbir *et al*., 2006). This route involves complexation of metal ions in EDTA/citric acid followed by solvent evaporation and thermal decomposition to form perovskite phase.

1.2.4 Hydrothermal

This method is still in its early stages of development. The process generally uses temperature between the boiling point of water and the material's critical temperature (i,e. 374 ºC) with the pressure as high as 15 MPa to produce advanced mixed oxides without calcinations steps. Several perovskite oxides were prepared using this technique because it is inexpensive and easy to control particle size, shape and stoichiometry (Zheng *et al*., 2000).

1.2.5 Spray and freeze drying

Spray drying is consisted of a rapid vaporization of the solvent in small fine droplets of cation solutions, whereas freeze drying involves the slow sublimation of the solvent in small frozen droplets. The purity, composition control and homogeneity are considered excellent. This technique can be scale up easily for manufacture of many muti-metallic oxides including perovskites.

Another method can be used to prepared perovskite and $LaFeO_3$ compound is the thermal decomposition of metal-organic complex which was first proposed as the decomposition of hexacyanocomplex by Gallagher in 1968 (Traversa *et al*., 1998). It is a simple technique for preparing these oxides with low cost, low processing temperature and low number of preparation steps (Farhadi *et al*., 2009). In addition, it was reported that this method is possible to prepare a single phase of trimetallic perovskite-type oxides containing either two rare earths or two transition metals at low temperature. This allows us to modulate the functional properties of perovskite oxides in a wide range. In this work, we used the thermal decomposition of metal-TEA complex to prepare $LaFeO_3$ and Sr(II) or Co(II) doped $LaFeO_3$ powders. The process consisted of the complexation between starting metal ions and TEA and calcination of the complexes to obtain the desired perovskite oxides.

1.3 Properties and applications

The vast variety of $LaFeO_3$ applications is due to the ability to control and design of the physical and chemical properties of prepared powders. In the detail, while the physical properties such as homogeneity, purity and particle size depend on preparation methods, the chemical properties of $LaFeO_3$ can be modified by substitution of other suitable cations at A, B or both sites to achieve substituted structure of $A_{1-x}A'_xB_{1-y}B'_yO_3$ which accounts for the large variety of catalytic reactions such as catalytic oxidation (Yang *et al*., 2007), hydrocarbon combustion (Asada *et al*., 2008), catalytic reduction (Lima *et al*., 2009) and photocatalytic reaction (Li et al., 2007).

In general, $LaFeO_3$ usually exits in non-stoichiometric forms because of the defections such as cation and anion vacancies in their structures. The presence of these imperfections associates with the reduction of Gibbs free energy by increasing entropy from defections and electrical balance from the fluctuation of two stable oxidation states, Fe^{2+} and Fe^{3+} (Sunarso *at al*., 2008). However, the compound with oxygen anion deficiency, $LaFeO_{3-\delta}$ is more common and very useful in catalysis because these vacancies increase the active sites of transition metals. Besides, it was reported that doping of lower valency cations such as Ca^{2+} or Sr^{2+} at the A-site can enhance catalytic activities of $LaFeO_3$ by increasing oxygen vacancies and unusual oxidation state of Fe^{4+} (Barbero *et al*., 2006; Leontiou *et al*., 2007). The $LaFeO_3$ and related perovskite-type oxides have many advantages in catalysis because of (Tanaka and Misono, 2001):

- the stability to high thermal and chemical conditions
- the stability of mixed oxidation states of transition metal in octahedral hole of oxygen
- the formation of unusual oxidation states when A- or B-site is substituted by another different valency ions
- the ability to control valency, vacancy and stoichiometry in wide range

Moreover, the $LaFeO_3$ has an interesting electrical property called mixed ionic-electronic conductivity which takes place by both of electron and ion transportations. In this case, oxygen vacancies also play the important role. The ionic conductivity usually occurs by the hopping of oxygen ions from one oxygen vacant site to neighboring vacant site, while the electronic conductivity arises via a B^{n+}-O-$B^{(n+1)+}$ conduction pairs to opposite direction for balancing charges as shown in Figure 2 (Sunarso *at al*., 2008). These properties allow the use of $LaFeO_3$ in many electronic devices such as electrode materials and oxygen permeation membranes (Sogaard *et al*., 2007; Bidrawn *et al*., 2010).

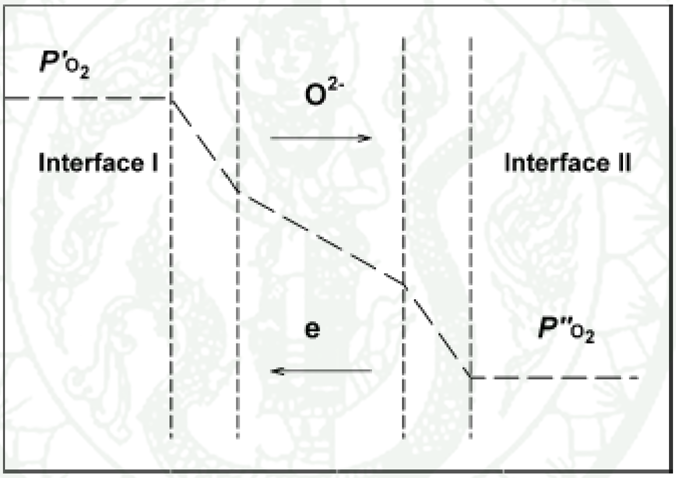

Figure 2 Conduction mechanism during oxygen permeation.

Source: Sunarso *at al.* (2008)

In addition, because of their catalytic and electronic properties, the $LaFeO_3$ has been proposed as the chemical sensing materials to detect toxic and combustible gases such as CO, CH_4, NO_2, NH_3, alcohol, acetone and LPG (Toan et al., 2003; Liu *et al*., 2006; Chaudhari *et al*.,2009). The sensitivity of sensing depends on physical and chemical properties of sensing materials directly, and however, although the $LaFeO_3$ can exhibit the high sensitivity to various kinds of gases, it has longer response time and has low selectivity. The response time and selectivity can be improved by addition of other metals such as Pb(II) (Song *et al*., 2005) at the A-site or another of the transition metals such as Cu(II) at the B-site (Song *et al*., 2009) to enhance the conductivity and catalytic activity of $LaFeO_3$. In this work, Sr(II) and Co(II) ions were used as a dopant to dope into the structure of $LaFeO_3$ in order to enhance sensing activity of $LaFeO_3$ and then its sensing properties to various kinds of gases such as C_2H_5OH, CH_3COCH_3 and CH_4 were studied.

2. Gas sensor applications

2.1 Semiconducting metal oxide gas sensors

Conductrometric gas sensors based on semiconducting metal oxides or semiconductor gas sensors are one of the most interested solid-state gas sensors which used to detect chemical gases such as CO, H_2, alcohols, propane, and other hydrocarbons. The vast current uses in large-scale of these type sensors are due to their advantages such as low cost, high sensitivity, large number of detectable gases and simplicity in their function and use. The comparison in sensing properties between semiconductor gas sensors and other types of sensors are shown in Table 1.

Table 1 Comparison of various types gas sensors

Parameter	Type of gas sensors				
	Semi-conductor	Catalytic combustion	Electro-chemical	Thermal conductive	Infrared absorption
Sensitivity	e	g	g	b	e
Accuracy	g	g	g	g	e
Selectivity	p	b	g	b	e
Response time	e	g	p	g	p
Stability	g	g	b	g	g
Cost	e	e	g	g	p

e: excellent, g: good, p: poor, b: bad

Source: Korotcenkov (2007)

In the working principle, when semiconductor gas sensors are exposed in oxidizing or reducing gas, the surface reactions between gas molecules and surface of metal oxide cause a change in their resistances and produce an electrical signal with a magnitude proportional to gas concentration. Due to this mechanism the sensing behavior of semiconductor gas sensors is therefore dependent on various kinds of gas involved in the surface reaction and also the type of semiconducting metal oxide. For example, in the presence of reducing gas, such as ethanol, the p-type semiconductor gas sensor's resistance is increased. Because the reduction reactions between ethanol gas molecules and the adsorbed oxygen ions on metal oxide surface release electrons as shown in equation (2) (Liu *et al*., 2008). These extra electrons are consequently recombined with the holes existing in p-type semiconductor. Since the concentration of hole decreased, the conductance is decreased and so the resistance is increased.

$$C_2H_5OH + 6O_2^- \text{(ads)} \longrightarrow 2CO_2 + 3H_2O + 12e^- \quad \text{------ (2)}$$

However, in spite of the simple working principle, the gas sensing mechanism involved is rather complex. The gas-semiconductor surface interactions occurring at the grain boundaries of the polycrystaliine oxide film generally include reduction/oxidation processes of semiconductor, adsorption of the chemical species on semiconductor surface, electronic transfer of delocalized conduction band electrons to localized surface states, surface chemical reactions between the different adsorbed chemical species and catalytic reactions as shown diagram in Figure 3 (Korotcenkov, 2007). These surface phenomena are significant change in electrical resistance and strongly depend on materials used. At present, there are many oxides have been used in semiconductor gas sensors, such as Fe_2O_3, SnO_2, ZnO, In_2O_3, WO_3, CuO and binary oxides including perovskites (Song *et al*., 2005; Wang *et al*., 2008), and sometimes, these sensing materials may be added with some additives such as noble and transition metals in order to improve the sensitivity and selectivity of sensors (Table 2).

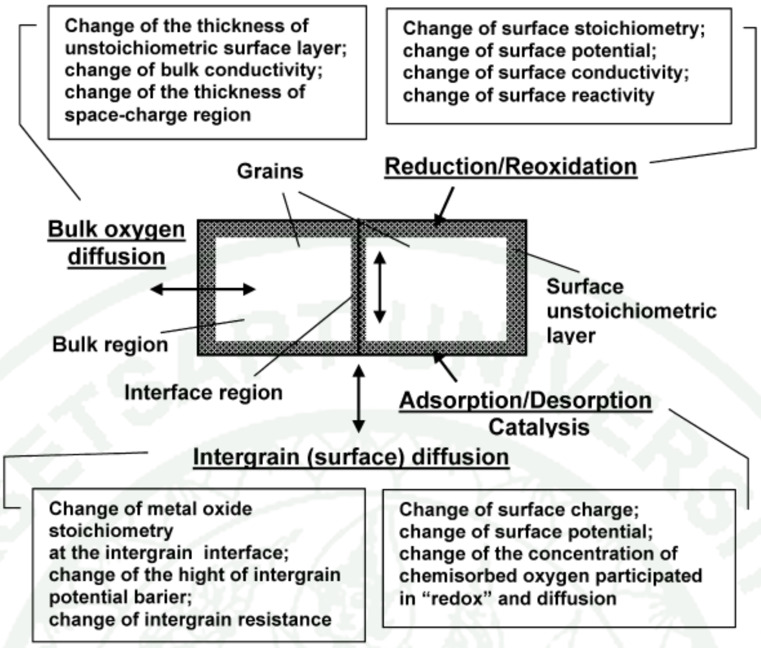

Figure 3 Diagram demonstrating processes occurring in metal oxides during gas detection.

Source: Korotcenkov (2007)

Table 2 Examples of semiconductor/additive/detected gas for semiconductor sensors

Semiconductor	Suggested additive	Gas to be detected
SnO_2	Pt + Sb	CO
SnO_2	Pt	Alcohols
SnO_2	Sb_2O_3 + Au	H_2, O_2, H_2S
WO_3	Pt	NH_3
Fe_2O_3	Ti-doped + Au	CO
ZnO	V, Mo	Halogenated hydrocarbons

Source: Sze (1994)

2.2 Spin coating technique

Spin coating is a simple technique commonly used for the film deposition of organic materials such as polyamides as well as inorganic oxides such as SnO_2. In this process, the material to be coated is formed into solution or paste with a volatile organic solvent. The material solution is poured on the substrate and then the substrate is readily spun at high speed rate of 2000-8000 rounds/minute for 10-60 seconds. While the liquid is spreading, the volatile organic solvent evaporates resulting in a uniform film as shown in Figure 4. The thickness of the film, which typically is in the range of 0.1 to 50 µm, depends on the degree of solubility and spin speed. The semiconductor gas sensors used in this work are also fabricated by this technique.

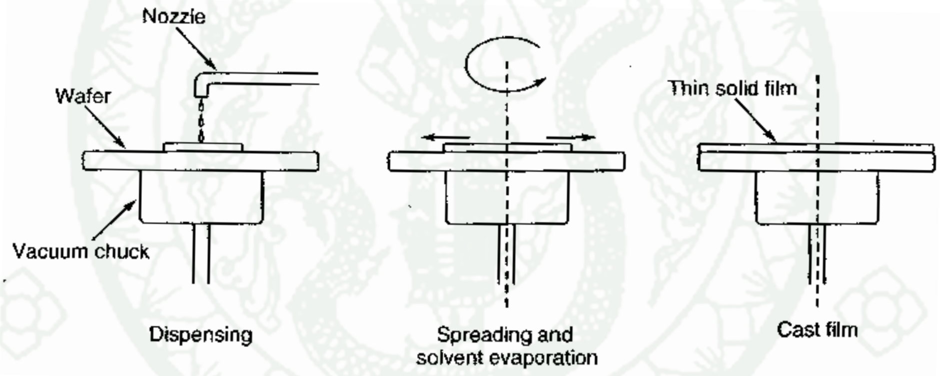

Figure 4 Spin coating process.

Source: Sze (1994)

OBJECTIVES

This work aims to study gas-sensing properties of un-doped, Sr(II) doped and Co(II) doped $LaFeO_3$ prepared by metal-organic complexes decomposition. Thus, there are four main objectives which are:

1. To synthesize the un-doped, Sr(II) doped and Co(II) doped $LaFeO_3$ by thermal decomposition of metal-organic complex using triethanolamine as a ligand.

2. To characterize the structure of prepared perovskite oxides by various techniques such as XRD, FTIR, SEM and BET.

3. To prepare the films of semiconductor gas sensor from perovskite powders by spin coating technique.

4. To study gas-sensing properties of un-doped, Sr(II) doped and Co(II) doped $LaFeO_3$ sensors to various kinds of gases such as ethanol, acetone, methane and hydrogen gas.

LITERATURE REVIEWS

This part is reviews of some previous works which has been researched by other researchers. It consists of preparation and characterization of the un-doped and doped $LaFeO_3$ by different methods. Moreover, some applications in gas sensor and the other relating works are also reviewed here.

Popa *et al*. (2003) prepared nanopowder of $LaFeO_3$ by polymerizable complex (PC) method. The obtained powder was characterized by X-ray diffraction (XRD), scanning electron microscope (SEM) and Raman spectroscopy. The results showed that homogeneous and single-phase perovskite with orthorhombic structure powder was obtained after calcined at 900 ºC for 6 h. SEM micrograph revealed an average particle size of about 80 nm and Raman spectrum could confirm the $LaFeO_3$ perovskite phase by the intensive line at 627 cm^{-1}.

Qi *et al*. (2003) prepared nanosized $LaFeO_3$ powder by sol-gel auto-combustion at room temperature. The $LaFeO_3$ powder was prepared in three steps which were formation of nitrate-citrate sol from $Fe(NO_3)_3 \cdot 9H_2O$, $La(NO_3)_3 \cdot 6H_2O$, $C_6H_8O_7 \cdot H_2O$ and $NH_3 \cdot H_2O$, formation of dried gel by heating to 130 ºC and auto-combustion of dried gel to as-synthesized powder in air at room temperature. From XRD spectra, they found that as-synthesized powder and powders obtained from dried gel directly heated at 700 and 1200 ºC for 2 h were $LaFeO_3$ phase with well-defined crystalline structure. The average particle size of as-synthesized powder was calculated to be 30 nm. The auto-combustion was considered as a heat-induced exothermic oxidation-reduction reaction between nitrate ions and carboxyl group.

Toan *et al*. (2003) studied the gas-sensing properties of $LaFeO_3$ thick films to CO, CH_4 and NO_2 gases. They found that the $LaFeO_3$ prepared by sol-gel method which had average particle size around 10 nm could be used as semiconducting gas sensor to detect CO and CH_4 concentrations in a few ten of ppm and NO_2 concentrations in the sub-ppm region. The prepared sensor had selective to different gases at different temperature which could use as an array of films to detect a gas mixture. The results showed that the sensor was most sensitive to CO in temperature range 250-270 ºC, to NO_2 at 350 ºC and to CH_4 at 420-450 ºC. The effects of two different kinds of electrodes were also investigated. They found that the $LaFeO_3$-based sensor with Au electrodes had a higher conductance than the similar sensor with Pt electrodes at lower temperature below about 400 ºC. In the other hand, the sensor with Pt electrodes could detect a gas sample with higher conductance than sensor with Au electrodes at high temperature.

Xiangfeng and Siciliano (2003) studied gas-sensing properties of $LaFeO_3$ thick-film to volatile sulfides. In their experiments, the $LaFeO_3$ was prepared by co-precipitation method. La_2O_3 dissolved in HNO_3 and $Fe(NO_3)_3{\cdot}4H_2O$ were mixed into de-ionized water and then added by 0.1 M NaOH to form precipitate. The co-precipitated powder was calcined at different temperatures of 600, 700, 800 and 900 ºC before tested with H_2S, CH_3SH and $(CH_3)_2S$. The results showed that the $LaFeO_3$ calcined at 700 ºC sensor exhibited higher sensitivity than any other and selective to CH_3SH at 250 ºC. However, it took a long response time.

Warnhus *et al*. (2004) studied the transport properties of cation and anion in $La_{0.9}Sr_{0.1}FeO_3$ compared with $LaFeO_3$ by secondary ion mass spectroscopy (SIMS). In their experiments, $La_{0.9}Sr_{0.1}FeO_3$ and $LaFeO_3$ were prepared with a glycine/nitrate technique. Y^{3+} and Cr^{3+} were used as tracer for A- and B-site diffusions by adding of $Y(NO_3)_3$ aqueous solution and an acidic solution of La_2CrO_6 in as-prepared solution. The results found that the diffusion of Cr on the B-site was faster than the diffusion of Y on the A-site. The activation energy acquired from the 10% Sr-doped $LaFeO_3$ was 150±30 kJ/mol for Cr diffusion and 168±24 kJ/mol for Y diffusion which lower than the results from $LaFeO_3$. It could conclude that the cation diffusion can easily occur in 10% Sr-doped $LaFeO_3$ compared with the cation diffusion in $LaFeO_3$.

Song *et al*. (2005) studied ethanol-sensing properties of $La_{1-x}Pb_xFeO_3$ perovskite ceramics. The $La_{1-x}Pb_xFeO_3$ (x = 0, 0.1, 0.2 and 0.3) were prepared by citric method and then calcined at 800 ºC for 3 h. The obtained powders were characterized by XRD before fabricating as gas sensors. The results from XRD showed that all the $La_{1-x}Pb_xFeO_3$ (x = 0, 0.1, 0.2 and 0.3) were perovskite phase with orthorhombic structure, and the mean crystallite size reduces with increasing Pb(II) content because Pb(II) ions could restrain the growth of grain size. In addition, they found that all the $La_{1-x}Pb_xFeO_3$ (x = 0, 0.1, 0.2 and 0.3) were p-type semiconducting material, and Pb(II)-doping could improve the conductivity of sensors by lowering the energy barrier of conduction. From gas testing, the results showed that $La_{0.8}Pb_{0.2}FeO_3$ sensor had the highest sensitivity to ethanol gas at an operating temperature of 140 ºC. Furthermore, the $La_{0.8}Pb_{0.2}FeO_3$-based sensor exhibited shorter response and recovery times than $LaFeO_3$-based sensor and also had good stability and durability after using for several months.

Barbero *et al.* (2006) studied the catalytic properties of $La_{1-x}Ca_xFeO_3$ for total oxidation of volatile organic compounds. The $La_{1-x}Ca_xFeO_3$ (x = 0, 0.2 and 0.4) were synthesized by citrate method using $Fe(NO_3)_3{\cdot}9H_2O$, $La(NO_3)_3{\cdot}6H_2O$, $Ca(NO_3)_2{\cdot}4H_2O$ and citric acid as reagents to prepared a gel precursor. The dried gel was milled and decomposed at 400 ºC for 30 min before calcined in air at 700 ºC for 2 h to acquire the $La_{1-x}Ca_xFeO_3$ powders. The powders were characterized by several techniques such as XRD, XRF, BET, FTIR, TPR and O_2-TPD. The results showed that the obtained powders were orthorhombic structure of perovskite phase with the specific surface area around 13-18 m^2/g. In addition, they found that the partial substitution for La^{3+} by Ca^{2+} caused the charge compensation by the oxygen vacancies and Fe^{4+} formations which associated to the active site for catalytic oxidation. The experiments on ethanol and propane combustions indicated that the conversion increased in the order $La_{0.8}Ca_{0.2}FeO_3 < LaFeO_3 < La_{0.6}Ca_{0.4}FeO_3$ which corresponded to the increasing of Fe^{4+} when the substitution increased.

Liu *et al.* (2006) found that $LaFeO_3$ thin films prepared by polymerization complex method had sensitivity to acetone gas with low concentration. In their work, $LaFeO_3$ precursor was prepared by using citric acid as a chelating agent to form complex with La and Fe ions in aqueous solution. The ethylene glycol was used as a cross-linking agent to promote polymerization of the citric acid by polyesterification reaction. After that $LaFeO_3$ precursor was coated on Al_2O_3 substrate by dip-coating and calcined at 650-750 ºC for complete crystallization. The $LaFeO_3$ thin film with thickness about 2 µm was tested with acetone gas. The results showed that the sensor could detect low concentration of acetone to 80 ppm which sensitivity was 204 and response time was 15 seconds as the testing temperature of 400 ºC.

Shabbir *et al*. (2006) synthesized nano-crystalline $LaFeO_3$ powder by the thermal decomposition of the gel complex of LaFe-($C_6H_8O_7 \cdot H_2O$). The gel complex was form by the reaction of $Fe(NO_3)_3 \cdot 9H_2O$, $La(NO_3)_3 \cdot 6H_2O$ and $C_6H_8O_7 \cdot H_2O$ and calcination of gel complex at different temperature. The optimum synthesis conditions was reported, using Differential Thermal Analysis (DTA), Thermogravimatic Analysis (TGA) and XRD. The results showed that the perovskite phase of $LaFeO_3$ powder was obtained at the crystallization temperature around 620 ºC, and the average particle size estimated by Hall-Williamson or Gaussian squared method was 29.33±1.31 nm.

Wang *et al*. (2006) prepared perovskite $LaFeO_3$ nanocrystal by glycine combustion method. In their work, the $LaFeO_3$ powder was prepared in two steps which were the reaction of $Fe(NO_3)_3 \cdot nH_2O$, $La(NO_3)_3 \cdot nH_2O$ and glycine in aqueous solution at 60-70 ºC and the ignition of mixture solution in air. The oxide product was characterized by XRD, transmission electron microscopy (TEM), Brunauer-Emmett-Teller (BET) nitrogen adsorption, UV-visible adsorption, Raman spectroscopy, energy dispersive X-ray spectrometer (EDS) and SEM. The results from XRD showed that the obtained $LaFeO_3$ powder was perovskite phase with orthorhombic structure which had calculated particle size about 25 nm corresponding to the TEM image. EDS and Raman spectroscopy confirmed the $LaFeO_3$ phase which composed of La, Fe and O with a mole ratio of 1 : 1 : 3 and exhibited band in Raman spectrum at around 150, 240, 430 and 610 cm^{-1}. The results from UV-visible adsorption exhibited that synthesized $LaFeO_3$ powder was a kind of photocatalytic material because of its adsorption peak at about 320 nm. The surface area of $LaFeO_3$ powder prepared by this technique was 7.9 m^2/g.

Yang *et al*. (2006) prepared highly ordered nanowires of $LaFeO_3$ using a citrate-based sol-gel method. The nanowire was synthesized by using a porous anodic aluminium oxide (AAO) and the highly ordered porous template with the hexagonal structure shape. In the experiment, $La(NO_3)_3 \cdot 6H_2O$, $Fe(NO_3)_3 \cdot 9H_2O$, $C_6H_8O_7 \cdot H_2O$ and $NH_3 \cdot H_2O$ was used as raw materials to prepared a homogeneous sol and then AAO template was immersed into the sol before heat treated at 953 K for 3 h to obtained $LaFeO_3$ nanowirres. SEM and TEM analysis revealed that the prepared nanowires were uniformly distributed with the size of 50 µm in length and outside diameter about 100 nm. XPS confirmed the stoichiometric $LaFeO_3$ composition of nanowire and the result from XRD indicated that the obtain nanowire was polycrystalline perovskite with an orthorhombic cell.

Jadhav *et al*. (2007) prepared $LaFeO_3$ at low temperature by using co-precipitation method. The preparation of $LaFeO_3$ powder consisted of two steps which were the formation of metal hydroxides from La_2O_3, $Fe(NO_3)_3 \cdot 4H_2O$ and NaOH solutions at 100ºC and the calcination at 450ºC for 6h. The results from XRD and TEM showed that the obtained powder was perovskite phase with orthorhombic structure and had an average particle size around 80 nm.

Dai *et al*. (2008) compared catalytic activities of $LaFeO_3$, $La_{0.8}Sr_{0.2}FeO_3$ and $La_{0.9}Sr_{0.1}Fe_{0.9}Co_{0.1}O_3$ for partial oxidation of CH_4. All three catalysts were prepared by sol-gel method using glycine in NH_3 as a reagent to form sol with metal nitrate solution. The sol solutions were evaporated into gels and then calcined at 900 ºC for 10 h. The results from XRD characterization showed that $LaFeO_3$, $La_{0.8}Sr_{0.2}FeO_3$ and $La_{0.9}Sr_{0.1}Fe_{0.9}Co_{0.1}O_3$ were orthorhombic $LaFeO_3$ structure with the crystallite size of 60.8, 34.6 and 32.9 nm, respectively. The experiments on CH_4 oxidation indicated that the CH_4 conversion increased in the order $LaFeO_3 < La_{0.8}Sr_{0.2}FeO_3 < La_{0.9}Sr_{0.1}Fe_{0.9}Co_{0.1}O_3$ which suggested that the amount of reactive oxygen species increased with A-site and B-site substitution.

Liu *et al*. (2008) studied the ethanol-sensing properties of $LaMg_xFe_{1-x}O_3$-based sensors. In their experiment, $LaMg_xFe_{1-x}O_3$ ($x = 0$, 0.1, 0.2 and 0.3) powders were synthesized by the sol-gel method using citric acid and then calcined at 800 ºC for 4 h before characterizing by XRD. The resistance and gas-sensing of the $LaMg_xFe_{1-x}O_3$-based sensors were also investigated. From the XRD results, they found that $LaMg_xFe_{1-x}O_3$ were perovskite-type $LaFeO_3$ phase when Mg content, x, was less than 0.3. In the case of x = 0.3, the La_2O_3 phase was observed. The Mg-doping decreased the resistance of $LaFeO_3$ and could improve the gas-sensing properties of $LaFeO_3$-based sensor. The gas testing results showed that $LaMg_{0.1}Fe_{0.9}O_3$-based sensor had selective to ethanol gas and exhibited the highest sensitivity at an operating temperature of 220 ºC.

Chaudhari *et al*. (2009) studied NH_3-sensing properties of $LaCo_xFe_{1-x}O_3$ (x = 0, 0.2, 0.4, 0.6 and 0.8) prepared by sol-gel citrate method using $La(NO_3)_3{\cdot}6H_2O$, $Fe(NO_3)_3{\cdot}9H_2O$, $Co(NO_3)_2{\cdot}6H_2O$ and citric acid as starting materials. The prepared gels were pre-heat at 350 ºC for 3 h and calcined 650 ºC for 6 h to obtain nanopowders. The results from XRD and TEM characterizations showed that the powders were an orthorhombic $LaFeO_3$ structure with the average grain size about 30-40 nm. After that the characterized powders were fabricated as thick film sensors for testing gas at different temperatures. The results indicated that the $LaCo_{0.8}Fe_{0.2}O_3$-based sensor exhibited the highest response to 200 ppm NH_3 at the operating temperature of 260 ºC. Compared with $LaFeO_3$, $LaCo_{0.8}Fe_{0.2}O_3$ showed the large response to NH_3 gas which might be due to the partial substitution of Fe^{3+} by Co^{2+} ions. In addition, the response characteristic of $LaCo_{0.8}Fe_{0.2}O_3$ to NH_3 gas also indicated that the $LaCo_{0.8}Fe_{0.2}O_3$ was p-type semiconductor which was improved the conductivity by holes generated from charge compensation.

Chu *et al*. (2009) studied trimethylamine sensing properties of nano- $LaFeO_3$ prepared by solid-state reaction in the presence of polyethylene glycol (PEG400). In their experiment, $La(NO_3)_3{\cdot}6H_2O$, $K_3[Fe(CN)_6]$ and PEG400 were ground together and then calcined at various temperatures of 400-900 ºC. The obtained powders were characterized by XRD and TEM before fabricated into thick film for measuring sensitivity to trimethylamine at different temperatures. The results from XRD indicated that the pure phase of $LaFeO_3$ was formed at 800 ºC. TEM images revealed about 50-80 nm of particle sizes which increased when the calcination temperature increased. The gas sensing results indicated that the sensor of $LaFeO_3$ calcined at 800 ºC exhibited the highest sensitivity to 1000 ppm trimethylamine at the operating temperature of 208 ºC with the maximum response value of 2553.

Farhadi *et al*. (2009) prepared $LaFeO_3$ nanoparticles by microwave-assisted decomposition of bimetallic $La[Fe(CN)_6]\cdot 5H_2O$ compound. The $La[Fe(CN)_6]\cdot 5H_2O$ was synthesized by mixing equivalent amounts of $K_3[Fe(CN)_6]$ and $La(NO_3)_3\cdot 6H_2O$ in aqueous solutions under stirring condition. After that the reddish-orange precipitate of $La[Fe(CN)_6]\cdot 5H_2O$ was obtained and then pressed into pellets before decomposed in a domestic microwave oven (2.45 GHz/ 900 W) for 4 min. The $LaFeO_3$ powder was characterized by XRD, FTIR, SEM, TEM and BET. The XRD and FTIR results indicated that the obtained powder was an orthorhombic $LaFeO_3$ structure with the crystallite size calculated by Debye-Scherrer around 28 nm. SEM micrograph showed the loosely aggregated grains about 1 μm in size, and the primary particle size about 30 nm was observed by TEM. Beside, BET result exhibited rather high specific surface area of powder prepared by this method which was 36.5 m^2/g.

Liu *et al*. (2009) studied the adsorption of O_2 on $LaFeO_3$ (010) surface with first-principles calculation based on density functional theory (DFT). From the experiment, they found that $LaFeO_3$ (010) surface was the La enrichment surface, but however, the sites of La and O on this surface were not the active sites for oxygen adsorption. The adsorbed O_2 on these La and O sites were not charge, and consisted of the O-O bond character denoting the physical adsorption of O_2. By contrast, the surface Fe ions were the active site and dominated the adsorption of oxygen gas. This corresponded with the experiment results that the catalytic activity of perovskite compound was essentially controlled by B-site metal. The adsorption between O_2 and Fe sites was considered as the strong interaction of the 2p orbital of adsorbed O_2 and 3d orbital of Fe ion. Finally, from the overall results, they concluded that the direct dissociation adsorption of O_2 was not observed, and in the other hand, the O_2 dissociation on $LaFeO_3$ (010) surface belonged to the chemisorbed-precursor mechanism. In this mechanism, the O_2 initially chemisorbed on Fe sites, and subsequently, the thermally driven kinetics determined the selectivity between desorption and dissociation. This was the reason that in experiments, $LaFeO_3$ needed to be heat to optimal temperature before the best gas response or catalysis was acquired.

Gosavi and Biniwale (2010) illustrated that the physical properties of $LaFeO_3$ depended on preparation method. In the experiment, they prepared $LaFeO_3$ by different three methods as shown in the reactions below;

co-precipitation:

$$La(NO_3)_3 + Fe(NO_3)_3 + NH_4OH \longrightarrow La(OH)_3 + Fe(OH)_3 + NH_4\,NO_3$$
$$La(OH)_3 + Fe(OH)_3 \longrightarrow LaFeO_3$$

glycine combustion:

$$La(NO_3)_3 + Fe(NO_3)_3 + 3.3H_2N(CH_2)CO_2H + 7.5\ O_2 \longrightarrow LaFeO_3 + 6.67CO_2 + 7.5H_2O + 1.67N_2$$

Citrate-based sol-gel:

$$La(NO_3)_3 + Fe(NO_3)_3 + C_6H_8O_7 \longrightarrow LaFeO_3 + 6CO_2 + 3N_2 + nH_2O$$

The $LaFeO_3$ powders were obtained by calcining all precursors at 800 ºC for 4 h via different heat cycles. XRD, SEM, EDS, FTIR and BET were used to characterize physical properties of prepared $LaFeO_3$. The results indicated that the combustion and sol-gel methods gave higher purity phase of $LaFeO_3$ than co-precipitation method which the prepared powder was contaminated by La_2O_3. The sol-gel method showed the highest surface area of 16.5 m^2/g with a porous surface while the combustion gave the lower of 9.3 m^2/g with flakes type morphology, and the co-precipitation exhibited the lowest surface area of 5.4 m^2/g with a more relative dense morphology.

MATERIALS AND METHODS

Materials

1. Chemicals

1.1 Lanthanum(III) nitrate hexahydrate ($La(NO_3)_3·6H_2O$); laboratory reagent grade, Fisher Scientific

1.2 Iron(III) nitrate nonahydrate ($Fe(NO_3)_3·9H_2O$); 98% analytical reagent grade, Ajax Finechem

1.3 Strontium(II) nitrate ($Sr(NO_3)_2$); laboratory reagent grade, Hi-Media

1.4 Cobalt(II) chloride ($CoCl_2·6H_2O$); laboratory reagent grade, Ajax Finechem

1.5 Triethanolamine (TEA, $N(CH_2CH_2OH)_3$); 80% laboratory reagent grade, Ajax Finechem

1.6 Ethylene glycol (EG, $HOCH_2CH_2OH$); 95% laboratory reagent grade, Ajax Finechem

1.7 Triton X-100; Fluka

1.8 Acetylacetone ($C_5H_8O_2$); 99.5% analytical reagent grade, Fluka

1.9 Ethanol (CH_3CH_2OH); 99.9% analytical reagent grade, Merck

1.10 Potassium bromide (KBr); IR grade, PIKE Technologies

2. Equipments

2.1 X-Ray Powder Diffractometer; Advance D8, Bruker-AXS

2.2 Fourier Transform Infrared Spectrometer; Perkin Elmer system 2000

2.3 Scanning Electron Microscope; XL30 & EDAX, Philips

2.4 Brunauer, Emmett and Teller (BET) Surface Analyzer; Autosorb 1C, Quantachrome Instruments

2.5 Thermal Gravimetric Analyzer; 761 Connecticut 06859, Perkin Elmer

2.6 Multimeter; 8846A G-1/2 digit precision multimeter, Fluke

2.7 Picoammeter; 6487 picoammeter/voltage source, Keithley

2.8 Mass flow; BROOKS 5850E, Brooks Instrument

2.9 Mass flow controller; Read Out & Control Electronics 0154, Brooks Instrument

2.10 Optical microscope

2.11 Spin coater

2.12 Furnace

2.13 Heating mantle

2.14 Desiccator

2.15 Laboratory Balance

Methods

1. Perovskite oxide preparation

1.1 Preparation of $LaFeO_3$, Sr(II) doped $LaFeO_3$ and Co(II) doped $LaFeO_3$ precursors

The precursor, metal-organic complex, of $LaFeO_3$ (LFO) was prepared by the chemical reaction of lanthanum(III) nitrate, iron(III) nitrate and triethanolamine (TEA) with the 1: 1: 3 mole ratio of La: Fe: TEA (Haron, 2005). In experiment, $La(NO_3)_3{\cdot}6H_2O$ 21.625 g (50 mmol), $Fe(NO_3)_3{\cdot}9H_2O$ 20.200 g (50 mmol) and TEA 19.80 ml (150 mmol) were mixed together into 180.00 ml of ethylene glycol solvent (EG). The mixture solution was heated at 190 ºC by a normal distillation manner as shown in Figure 5, and during the reaction progress, small amount of EG was carefully filled into the solution in order to compensate the remaining EG which was continually distilled to be a distillate with by-products such as NO_x and H_2O. The reaction was complete in five hours, and the precipitate product in dark brown solution residues was separated by filtration and then washed twice with ethanol before dried at 80 ºC to obtain the pale yellow powder of $LaFeO_3$ precursor.

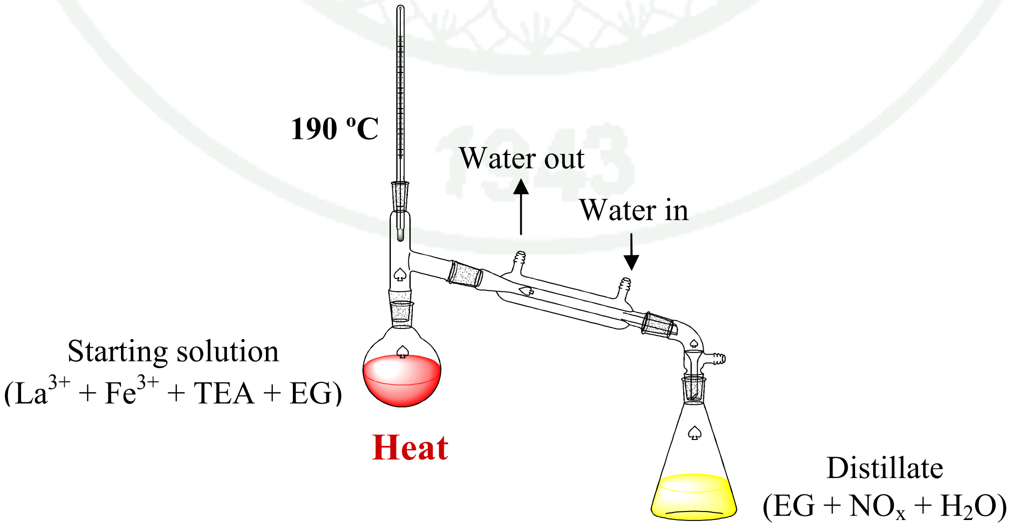

Figure 5 A normal distillation procedure for $LaFeO_3$ precursor preparation.

For preparation of 10, 30 and 50% Sr(II) doped $LaFeO_3$ precursors, $Sr(NO_3)_2$ used as a dopant was added into the starting solution with an appropriate amount of La, Fe and TEA as shown in Table 3. And after the same preparing process as mention above was applied, the Sr(II) doped $LaFeO_3$ precursor was obtained into the form of pale yellow powder. Similarly, the precursors of 10, 30 and 50% Co(II) doped $LaFeO_3$ were also prepared by this procedure. In this case, $CoCl_2{\cdot}6H_2O$ was used as a dopant (Table 4), and the pale yellow powder of Co(II) doped $LaFeO_3$ precursor was acquired. At last, all of perovskite oxide precursors were ground into fine powder and characterized by TGA.

Table 3 The amount of starting materials for 50 mmol of Sr(II) doped $LaFeO_3$ precursors preparation

Perovskite oxides	Amount of starting materials			
	$La(NO_3)_3{\cdot}6H_2O$ (g)	$Fe(NO_3)_3{\cdot}9H_2O$ (g)	TEA (ml)	$Sr(NO_3)_2$ (g)
$La_{0.9}Sr_{0.1}FeO_3$ (LSFO10)	19.486 (45 mmol)	20.200 (50 mmol)	19.80 (150 mmol)	1.058 (5 mmol)
$La_{0.7}Sr_{0.3}FeO_3$ (LSFO30)	15.156 (35 mmol)	20.200 (50 mmol)	19.80 (150 mmol)	3.174 (15 mmol)
$La_{0.5}Sr_{0.5}FeO_3$ (LSFO50)	10.826 (25 mmol)	20.200 (50 mmol)	19.80 (150 mmol)	5.291 (25 mmol)

Table 4 The amount of starting materials for 50 mmol of Co(II) doped $LaFeO_3$ precursors preparation

Perovskite oxides	Amount of starting materials			
	$La(NO_3)_3{\cdot}6H_2O$ (g)	$Fe(NO_3)_3{\cdot}9H_2O$ (g)	TEA (ml)	$CoCl_2{\cdot}6H_2O$ (g)
$LaFe_{0.9}Co_{0.1}O_3$ (LFCO10)	21.652 (50 mmol)	18.180 (45 mmol)	19.80 (150 mmol)	1.190 (5 mmol)
$LaFe_{0.7}Co_{0.3}O_3$ (LFCO30)	21.652 (50 mmol)	14.140 (35 mmol)	19.80 (150 mmol)	3.569 (15 mmol)
$LaFe_{0.5}Co_{0.5}O_3$ (LFCO50)	21.652 (50 mmol)	10.100 (25 mmol)	19.80 (150 mmol)	5.948 (25 mmol)

1.2 Preparation of $LaFeO_3$, Sr(II) doped $LaFeO_3$ and Co(II) doped $LaFeO_3$ powders

To obtain perovskite oxide powders, the $LaFeO_3$, Sr(II) doped $LaFeO_3$ and Co(II) doped $LaFeO_3$ precursors were calcined at selected temperature determined by thermal gravimetric analysis (TGA) in order to remove organic contents. Hence, each of precursors was loaded into an alumina crucible and then calcined at 850 ºC by using a box furnace with the heating rate of 3.4 ºC/min for 4 hours under atmospheric condition (Haron, 2005). Finally, the calcined product was ground into fine powder and then characterized by XRD, FTIR, SEM and BET.

1.3 Characterization of $LaFeO_3$, Sr(II) doped $LaFeO_3$ and Co(II) doped $LaFeO_3$ precursors and powders

1.3.1 Thermal Gravimetric Analysis (TGA)

In this work, the TGA technique was used to study the thermal decomposition behavior and determine the crystallization temperature of metal-organic complexes. At the beginning, a thermal gravimetric analyzer was set as a sample zero state by the weight of a platinum pan contained with about 5.000 mg of alumina powder, a refractory material used to prevent the pan from damage. After that, about 8.00-10.00 mg of sample powder was loaded into that pan and then run at the temperature range of 50.0-1000.0 ºC with the heating rate of 10.0 ºC/min to obtain a thermogram of the sample.

1.3.2 Fourier Transform Infrared Spectroscopy (FTIR)

The FTIR technique was used to characterize the organic component in the obtained precursors. To acquire an FTIR spectrum, small amount of dried sample powder was mixed together with about 0.500 g of KBr, a specially purified salt which does not absorb IR radiation, and ground into homogeneous, fine powder. The mixture powder was pressed in a mechanical die to form a pellet and then scanned with IR radiation to collect the percentage of transmittance from the wavenumber of 4000 cm^{-1} to 400 cm^{-1}.

1.4 Characterization of $LaFeO_3$, Sr(II) doped $LaFeO_3$ and Co(II) doped $LaFeO_3$ powders

1.4.1 X-Ray Powder Diffraction (XRD)

The crystal structure of all perovskite oxide powders was investigated by an X-ray powder diffractometer which used CuKα radiation as an X-ray source (λ = 1.5406 Å) operated at 40 kV 40 mA. For an analysis, about 2.00 g of the sample powder was spread on a sample stub and then pressed by a slide glass to smooth its surface. After that, the stub was fixed into a sample holder and scanned from 2θ of 20.00° to 90.00° with the scan step was 0.04° to acquire an XRD pattern. The crystal structure was identified by comparing the XRD pattern of the sample with a standard pattern, the JCPDS (Joint Committee on Powder Diffraction Standards) file, and lattice parameters of the unit cell could be calculated by the relationship of an orthorhombic system as shown below (Hammond, 2001);

$$\frac{1}{d_{hkl}^2} = \frac{h^2}{a^2} + \frac{k^2}{b^2} + \frac{l^2}{c^2} \qquad \text{------ (3)}$$

Where h, k, l are the miller indices of a lattice plane

d_{hkl} is the interplanar spacing between planes (h k l)

a, b, c are lattice parameters or unit cell parameters of an orthorhombic system ($a \neq b \neq c$)

These parameters represent three dimensional lengths of the unit cell. Hence, the unit cell volume can be calculated by

$$V = abc \qquad \text{------ (4)}$$

Whence V is the unit cell volume of an orthorhombic system

a, b, c are the unit cell parameters of an orthorhombic system

In addition, the crystallite size of perovskite oxide powders was calculated from data of the highest peak in the XRD pattern by using Scherrer equation (Hammond, 2001) which is generally written by

$$t = \frac{K\lambda}{\beta \cos\theta} \qquad \text{------ (5)}$$

Where t is the crystallite size or grain size of polycrystalline powder (nm)

λ is the wavelength of an X-ray source (nm)

θ is the Bragg angle of a selected diffraction peak (degree)

K is an estimate of the shape correction factor, a constant which approximately is 0.9

β is the full width at half maximum (FWHM) of a selected diffraction peak (radians)

The FWHM of the selected diffraction peak was determined by using a fityk program, a free software program for nonlinear fitting method, to fit the diffraction data with a Lorentzian function (Abdullah and Khairurrijal, 2008). However, although the band broadening can reflect the thickness or size of crystalline materials, the measurement of ‘absolute grain sizes’ is rather difficult because of the presence of the other factors which contribute to the broadening of the XRD peak such as imperfections, lattice strains and instrumental broadenings. Thus, the calculated crystallite sizes in this work could be regarded as only the ‘estimated crystallite size’ or ‘relative crystallite size’ for comparison between prepared oxides in the same series.

1.4.2 Fourier Transform Infrared Spectroscopy (FTIR)

The FTIR technique was used to confirm the perovskite structure of prepared powders. To acquire an FTIR spectrum, small amount of dried sample powder was mixed together with about 0.500 g of KBr, a specially purified salt which do not absorb IR radiation, and ground into homogeneous, fine powder. The mixture powder was pressed in a mechanical die to form a pellet and then scanned with IR radiation to collect the percentage of transmittance from the wavenumber of 4000 to 400 cm^{-1}.

1.4.3 Scanning electron microscopy (SEM)

The surface morphology of prepared oxide powders was studied on a scanning electron microscope. For SEM operation, the sample powder was spread on a carbon tape which mounted on a sample stub and then coated by a small layer of gold in order to enhance conductivity. After that, the sample was scanned by 13.0 keV of electron beam in high vacuum to obtain an SEM image with the magnification of 5000 and 10000.

1.4.4 Brunauer, Emmett and Teller surface analysis (BET)

The surface area analysis of prepared oxide powders was carried out on a BET surface analyzer. To acquire the specific surface area, about 2.000 g of sample powder was outgassed at 300 ºC for 15 hours and then studied BET adsorption isotherm with nitrogen gas adsorption at 77 K.

2. Sensor fabrication

2.1 Fabrication of $LaFeO_3$, Sr(II) doped $LaFeO_3$ and Co(II) doped $LaFeO_3$ sensors

For fabricating a sensor, the film of perovskite oxides was deposited on an alumina substrate (3 x 4 mm) with gold interdigitated electrodes by spin coating technique as illustrated in Figure 6. Originally, 20.0 µl of triton X-100 binder and 60 mg of prepared oxide powder was mixed and ground together in small amount of acetylacetone solvent to form a uniform paste. After that, the paste was dropped on the alumina substrate and then spun by a spin coater with the spin rate of 3000 rounds/min for 30 seconds to form the film which was consequently annealed at 500 ºC for 2 hours in order to remove organic contents.

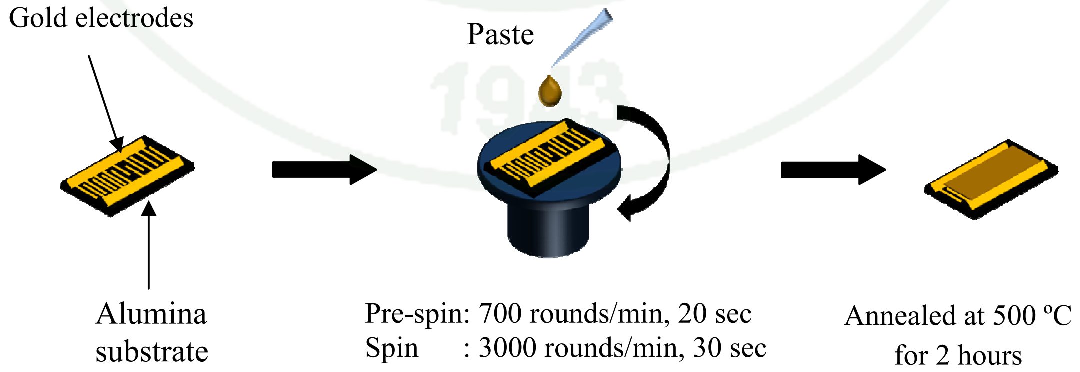

Figure 6 A schematic diagram of sensor fabrication by spin coating technique.

2.2 Characterization of $LaFeO_3$, Sr(II) doped $LaFeO_3$ and Co(II) doped $LaFeO_3$ sensors

2.2.1 X-Ray Powder Diffraction (XRD)

The film sensors were characterized by an X-ray powder diffractometer operated at 40 kV 40 mA for confirming that the perovskite phase still remained in the oxide films. To characterize, the sensor was mounted on a sample stub by an adhesive tape before placed in a sample holder and then scanned with CuKα radiation ($\lambda = 1.5406$ Å) from 2θ of 20.00° to 90.00° with the scan step was 0.04°. Lastly, the obtained XRD pattern was identified by comparison to JCPDS file no. 37-1493 ($LaFeO_3$), JCPDS file no.82-1467 (Al_2O_3) and JCPDS file no.04-0784 (Au).

2.2.2 Scanning electron microscopy (SEM)

The surface morphology of film sensors was studied on a scanning electron microscope. For SEM operation, the sensor was mounted on a sample stub by a carbon tape and then coated by a small gold layer in order to enhance conductivity. After that, the sensor was scanned by 13.0 keV of electron beam in high vacuum to obtain a SEM image with the magnification of 5000.

2.2.3 Optical microscopy (OM)

The thickness of film sensors prepared by spin coating technique was evaluated on an optical microscope. To obtain an image of the film thickness, the sensor was perpendicularly fixed on a slide glass by an adhesive material and then mounted on a specimen stage. Subsequently, the microscope was operated on a suitable magnification giving the best image, and after that, the satisfied image was captured by photographing with a digital camera. At last, the thickness of the film was estimated by a relative scale in the image obtained at the magnification of an objective lens was 5x and the magnification of an eyepiece was 10x.

3. Gas-sensing properties measurement

The gas-sensing characteristics of prepared sensors based on semiconducting metal oxide were investigated by measuring a change of sensors' electrical resistance in the presence of sample gas. In a gas testing chamber, the gold electrodes of a sensor were contacted with the probe on a heating state. The heating voltage was applied to two Ni-Cr coils under the heating state for heating up the sensor, and the operating temperature was detected by a thermo couple.

For gas testing, the adjustable operating voltage was supplied across the sensor through the probe, and the sensor's resistance was measured by a multimeter or picometer. The sample gas was injected into the chamber by a mass flow controller using air zero as a carrier gas. All of operating steps was performed by a computer's software, and a diagram which illustrates the gas testing is shown in Figure 7.

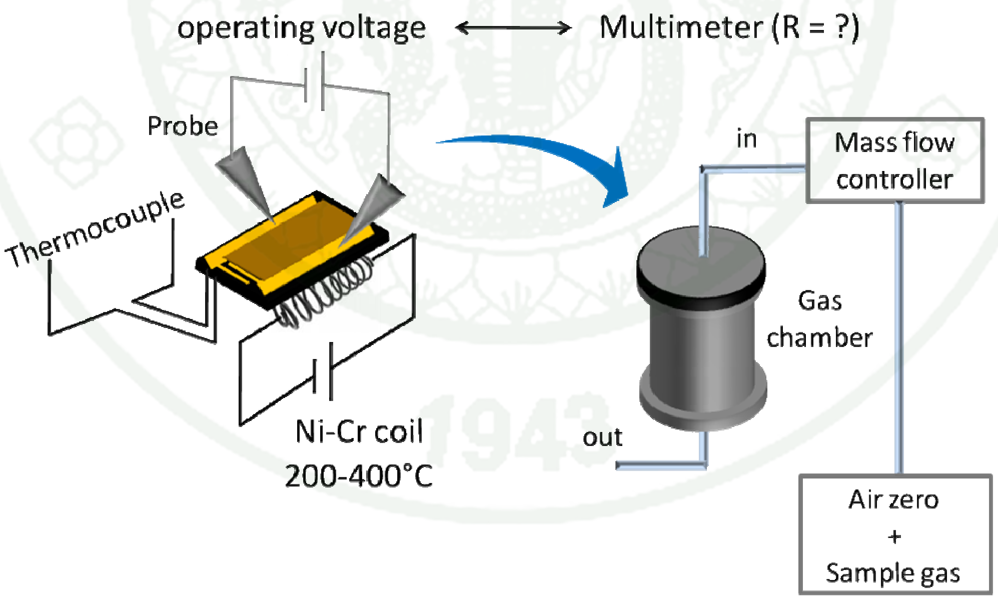

Figure 7 A schematic diagram of gas-sensing measurement.

To determine the sensitivity of sensors, the resistance of the gas sensor was measured at various operating temperature (250-400 ºC). The sensitivity of sensors was expressed in term of response (R) which defined by

$$R = \frac{R_g}{R_a} \qquad \text{------ (6)}$$

Where R_g is the sensor’s resistance in the presence of sample gas
R_a is the sensor’s resistance in air zero

In this work, the responses of un-doped $LaFeO_3$, Sr(II) doped $LaFeO_3$ and Co(II) doped $LaFeO_3$ sensors to various concentrations of sample gases such as ethanol, acetone, hydrogen and methane were investigated.

RESULTS AND DISCUSSIONS

1. Perovskite oxide preparation

1.1 Characterization of $LaFeO_3$, Sr(II) doped $LaFeO_3$ and Co(II) doped $LaFeO_3$ precursors

1.1.1 Thermal Gravimetric Analysis (TGA)

All perovskite oxide precursors exhibited quite similar TGA thermogram with three weight loss regions of thermal decomposition as shown in Figure 8. This representative TGA thermogram, LFO precursor exhibited the first weight loss at the temperature range of 50 ºC to 200 ºC which referred to the removal of water and the remaining organic solvent. The second weight loss from 200 ºC to 500 ºC corresponded to the decomposition of organic contents, and the last weight loss at 500-700 ºC was attributed to the elimination of carbon residues (Kazak *et al*., 2003; Biswas *et al*. 2008). After 700 ºC, no weight loss was observed indicating that all organic contents were removed, and the precursor was completely converted to oxide powder with about 50% of ceramic yield. Therefore, the prepared perovskite oxide precursors were calcined at 850 ºC for 4 hours to ensure that the perovskite phase was obtained.

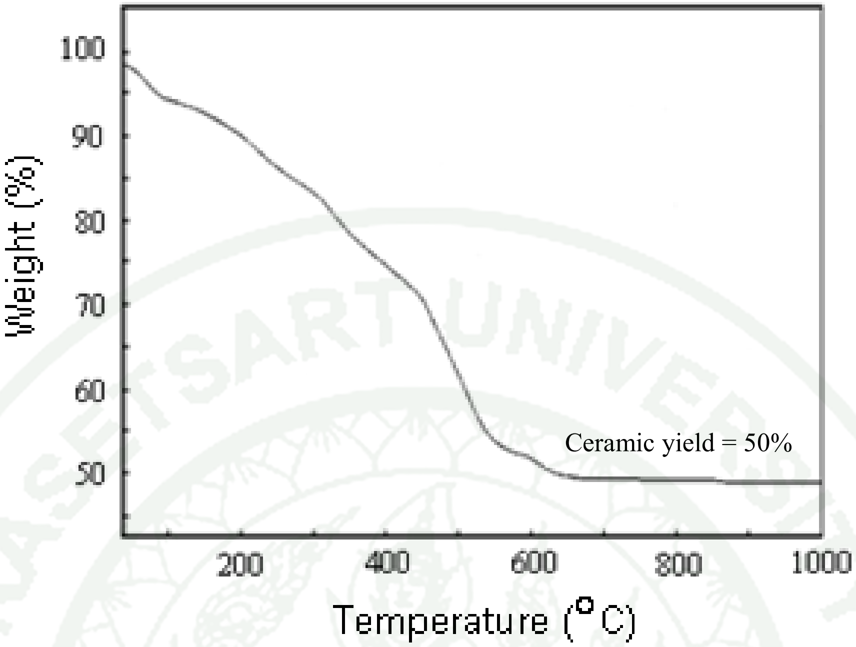

Figure 8 TGA thermogram of LFO precursor.

1.1.2 Fourier Transform Infrared Spectroscopy (FTIR)

The organic contents in perovskite oxide precursors were characterized by FTIR spectroscopy. Figure 9 shows the infrared spectra of a ligand, triethanolamine (9-a) and LFO precursor (9-b). It can be seen that almost of absorption peaks in the LFO precursor spectrum corresponded to the characteristic absorption peaks of triethanolamine (Table 5).

In LFO precursor spectrum, the broad band at around 3382 cm^{-1} was assigned to the stretching of OH groups. The very weak band around 2950-2870 cm^{-1} correlated with the absorption of C-H stretching vibration, and the small peaks at about 935 and 1074 cm^{-1} corresponded to the stretching of C-O and C-N, respectively. In addition, the small absorption peak at 518 cm^{-1} might be due to M-O or M-N stretching of metal coordinated with triethanolamine ligand. Consequently, the C-O and C-N stretching of coordinating ligand shifted to lower frequencies denoting the formation of metal-organic complex (Kazak *et al*., 2003; Karadag *et al*., 2001;

Nakamoto, 1997). The FTIR results of other precursors also gave the similar spectrum of LFO precursor.

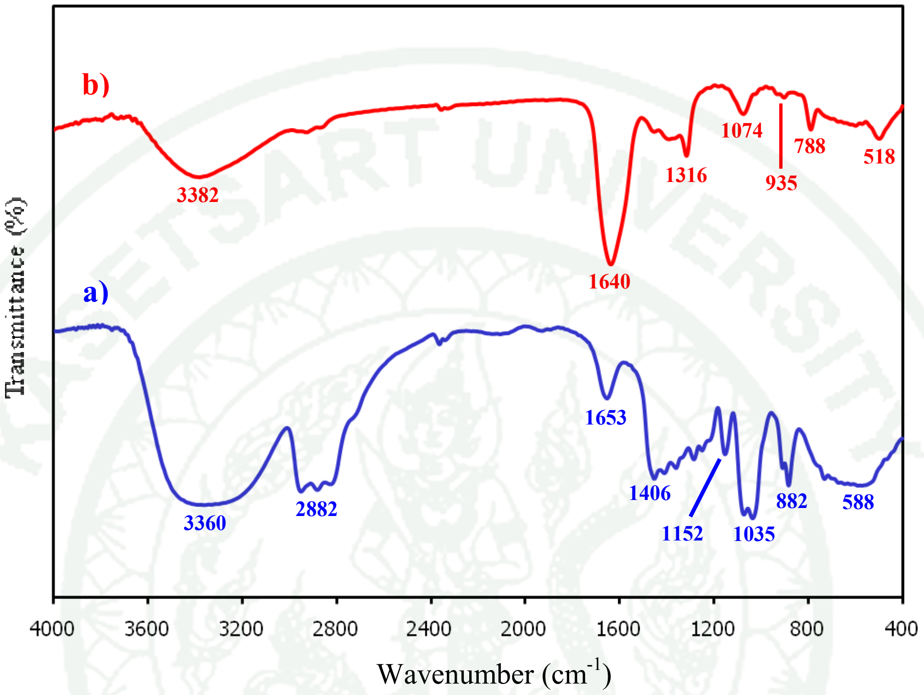

Figure 9 FTIR spectra of a) triethanolamine and b) LFO precursor.

Table 5 FTIR spectral data of triethanolamine and LFO precursor

Band assignment	Wavenumber (cm^{-1})	
	Trietanolamine	LFO precursor
ν (O-H)	3550-3200 vb	3380 b
ν (C-H)	2900-2850 s	2950-2870 vw
δ (CH_2)	~1460-1300 w	~1477-1325 w
ν (C-N)	1152 m	1074 w
ν (C-O)	1035 s	935 vw
ν (M-O), ν (M-N)	-	518 w

vb = very broad, b = broad, s = strong, m = medium, w = weak, vw = very weak

From the results of TGA and FTIR, It could be concluded that the prepared perovskite oxide precursors were metal-organic complexes containing triethanolamine as ligand. However, the attempt to recrystallize metal-organic complex precursors failed because of their high stability and undissolved in any solvent such as methanol, ethanol, acetone, hexane, acetonitrile, dichloromethane, ethyl acetate or chloroform. Thus, further characterizations and their structures could not be performed.

1.2 Characterization of $LaFeO_3$, Sr(II) doped $LaFeO_3$ and Co(II) doped $LaFeO_3$ powders

1.2.1 X-Ray Powder Diffraction (XRD)

After calcined at 850 ºC for 4 hours, the precursors were converted into yellowish, blackish and brownish powders of $LaFeO_3$, Sr(II) doped $LaFeO_3$ and Co(II) doped $LaFeO_3$ perovskite oxides, respectively. Thereafter, the obtained oxide powders were characterized by XRD to confirm their crystal structures, and the results revealed that all of prepared oxide powders were perovskite phase with orthorhombic structure.

Figure 10 shows XRD patterns of the un-doped and Sr(II) doped $LaFeO_3$ powders. It can be seen that all diffraction peaks agreed well with a JCPDS file no. 37-1493 referring to the orthorhombic structure of $LaFeO_3$ phase. The sharpness and rather high intensity of the peaks revealed the well-crystallized prepared powders, and interestingly, a small shift to higher 2-theta values of diffraction peaks was observed when the amount of Sr(II) dopant increased demonstrating that doped Sr(II) ions slightly affected on the d-spacing values of $LaFeO_3$ structure as summarized in Table 6. In addition, although the results from XRD obviously confirmed the $LaFeO_3$ phase of prepared powders, the minor impurity phase of $SrLaFeO_3$ was detected, particularly in the higher quantities of Sr(II) as in LSFO30 and LSFO50 (Berger *et al*., 2010).

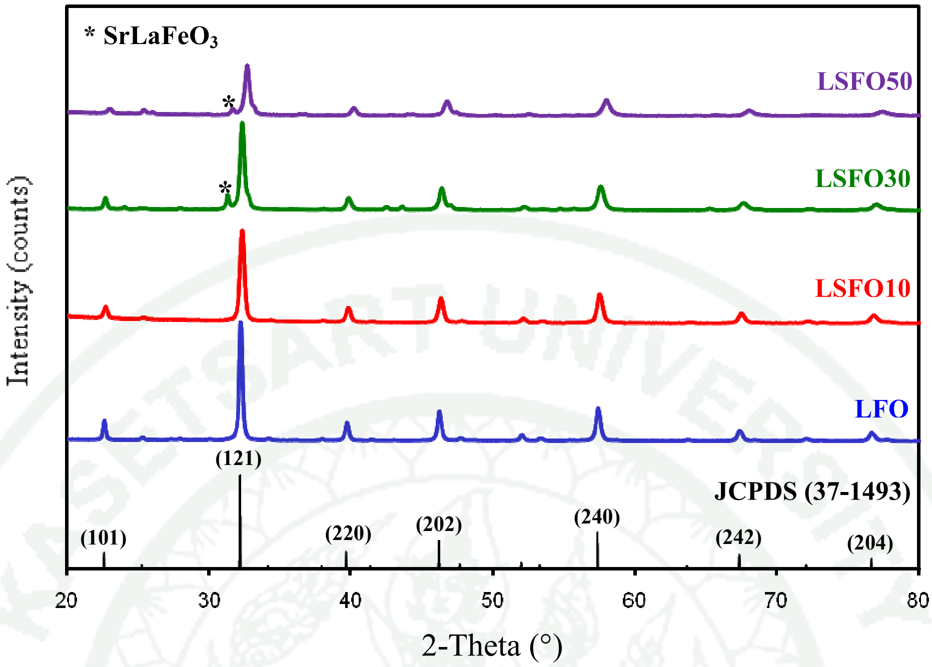

Figure 10 XRD patterns of the un-doped and Sr(II) doped $LaFeO_3$ powders.

Similarly, the XRD patterns of all Co(II) doped $LaFeO_3$ (Figure 11) show the $LaFeO_3$ phase with orthorhombic structure, corresponding to a JCPDS file no. 37-1493. However, as the increasing amounts of Co(II) dopant up to 30-50% mol, a slight shift to higher 2-theta values of the peaks was observed and small impurities of La_2O_3, Co_3O_4 and CoO phases were also detected as shown in the XRD pattern of LFCO50 (Dai *et al*., 2008). The data of the main diffraction peaks of the prepared powders such as 2-theta and d-spacing values were summarized in Table 6.

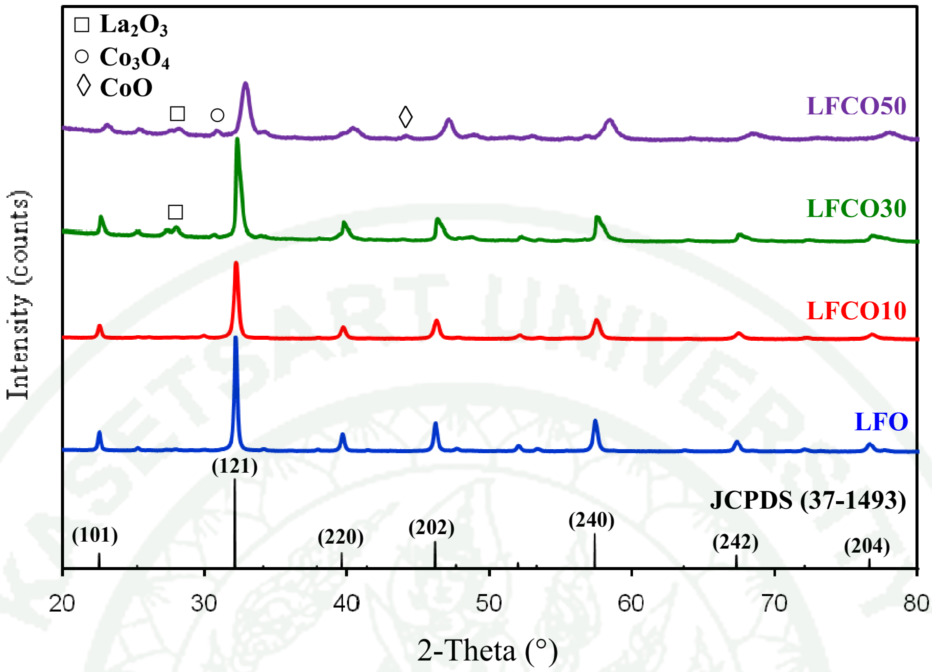

Figure 11 XRD patterns of the un-doped and Co(II) doped $LaFeO_3$ powders.

Table 6 Diffraction angle (2θ), d-spacing values (d) and relative intensity (I/I_0) of three main diffraction peaks obtained from XRD patterns of the un-doped, Sr(II) doped and Co(II) doped $LaFeO_3$ powders.

Perovskite oxide	Diffraction peak (h k l)								
	121			240			202		
	2θ (°)	d (Å)	I/I_0 (%)	2θ (°)	d (Å)	I/I_0 (%)	2θ (°)	d (Å)	I/I_0 (%)
JCPDS file no. 37-1493	32.188	2.7860	100	57.395	1.6080	39	46.141	1.9710	30
LFO	32.221	2.7828	100	57.442	1.6069	25.89	46.208	1.9679	23.35
LSFO10	32.311	2.7752	100	57.542	1.6044	25.47	46.310	1.9638	25.19
LSFO30	32.325	2.7740	100	57.626	1.6022	28.51	46.378	1.9610	24.86
LSFO50	32.674	2.7452	100	58.027	1.5920	31.55	46.757	1.9460	28.04
LFCO10	32.254	2.7800	100	57.535	1.6045	24.94	46.273	1.9653	23.98
LFCO30	32.420	2.7662	100	57.743	1.5992	23.19	46.481	1.9570	21.28
LFCO50	32.913	2.7258	100	58.435	1.5820	35.06	47.132	1.9314	34.54

Peak fitting of all diffraction peaks was performed by using the Lorentzian function.

From the XRD results, it was obvious that both of Sr(II) and Co(II) doping had an effect on the structure of $LaFeO_3$ by lowering d-spacing values. The calculation from XRD data exhibited that lattice parameters of the prepared $LaFeO_3$ slightly decreased when the amounts of Sr(II) or Co(II) increased resulting in the reduction of unit cell volume (Table 7). These phenomena could be explained by the formations of oxygen vacancies and Fe^{4+} ions (Song *et al*., 2005; Barbero *et al*., 2006). Consider, for example, in the case of Sr(II) doping, when La^{3+} was substituted by Sr^{2+} ion at the A-site of $LaFeO_3$, the charge compensation could be occurred in order to maintain the neutrality by several ways. One was the loss of oxygen in the structure causing oxygen vacancies and unit cell shrinkage consequently. Besides this, the charge could be neutralized by the formation of Fe^{4+} ions, and this, probably, also contributed to the causing of a change on unit cell parameters because the size of Fe^{4+} is smaller than that of Fe^{3+} ion. However, if we consider the ionic radii of metal ions as shown in Table 8, it is seen that the size of Sr^{2+} and Co^{2+} dopants are slightly different from those of doping site, La^{3+} and Fe^{3+}. It suggests that size effect may cause a minor change to the unit cell parameters. To maintain the change and normal structure of perovskite phase, oxygen vacancies formation is then predominant effect to the unit cell volume. Therefore, as increasing the amounts of Sr(II) or Co(II) doped in A- or B-site of $LaFeO_3$, the unit cell volume becames smaller.

It is evidenced by the crystallite sizes of the prepared powders decreased when the amounts of Sr(II) or Co(II) increased, especially in the case of LFCO50 as illustrated in Table 7. This demonstrated that doping Sr(II) or Co(II) ions could retard the grain growth of $LaFeO_3$ (Song *et al*., 2005).

Table 7 Lattice parameters (a, b, c), unit cell volume (V) and crystallite size (t) of the un-doped, Sr(II) doped and Co(II) doped $LaFeO_3$ powders

Perovskite oxide	Lattice parameters[a]			V (Å^3)	t (nm)[b]
	a (Å)	b (Å)	c (Å)		
LFO	5.5692	7.8702	5.5628	243.82	41.892
LSFO10	5.5800	7.8440	5.5290	242.00	33.075
LSFO30	5.5520	7.8481	5.5414	241.45	26.763
LSFO50	5.5942	7.7455	5.4184	234.77	23.140
LFCO10	5.5521	7.8650	5.5651	243.01	29.944
LFCO30	5.5608	7.8201	5.5098	239.60	25.501
LFCO50	5.5620	7.6939	5.3690	229.76	14.312

[a] Calculated from XRD data of three main diffraction peaks (see Appendix C).

[b] Calculated from Scherrer equation (see Appendix D).

Table 8 Effective ionic radii of some metal ions

Ion	Coordination number	Ionic radii (pm)
La^{3+}	12	150
Sr^{2+}	12	158
Fe^{3+}	6	78.5
Fe^{4+}	6	72.5
Co^{2+}	6	88.5

Source: Huheey (1993)

1.2.2 Fourier Transform Infrared Spectroscopy (FTIR)

FTIR spectra of the prepared powders provided the significant information of M-O bond in far-IR region. Figure 12 shows FTIR spectra of the un-doped and Sr(II) doped $LaFeO_3$ powders which exhibited the absorption frequency of Fe-O stretching around 590-610 cm^{-1}. This vibration is a characteristic of FeO_6 octahedron in $LaFeO_3$ structure (Gosavi and Biniwale, 2010). The other bands in the spectra revealed small residual phases of prepared powders. For example, the absorption peak at about 2366 cm^{-1} was attributed to the physically surface-adsorbed CO_2, but this band is generally observed in an IR spectrum. The weak bands around 1565 and 1440 cm^{-1} were more interesting. It corresponded to the vibration of CO_3^{2-} group of carbonate compounds denoting the small impurities of the precursor oxidation in preparing step (Wei *et al*., 2009). However, this contamination was slightly observed only in the case of high quantities of Sr(II) were doped, such as LSFO50.

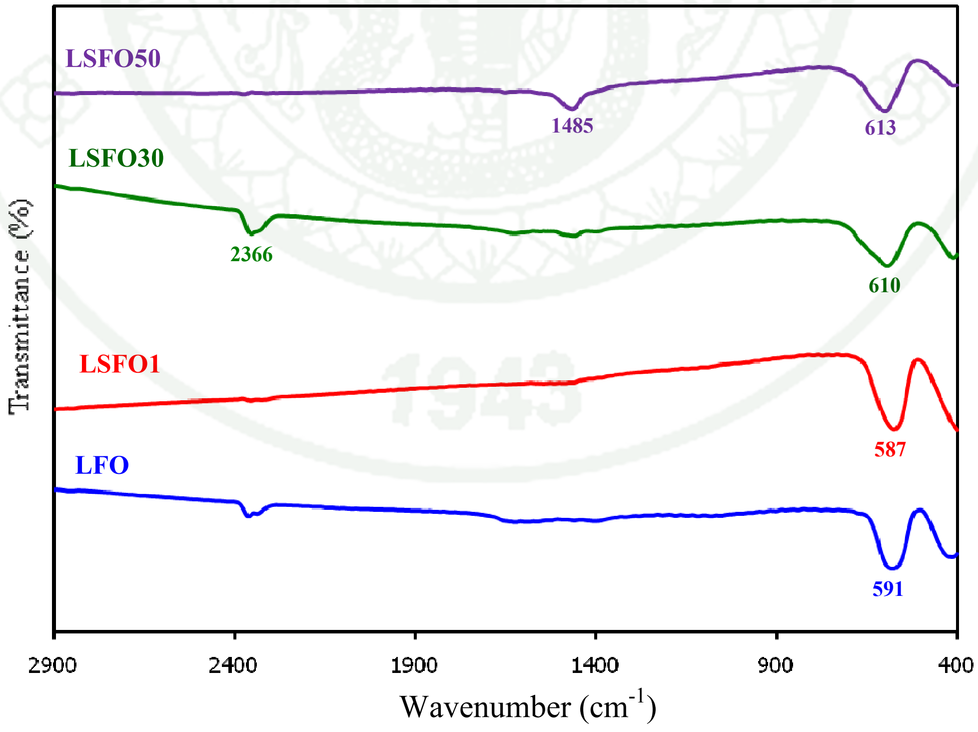

Figure 12 FTIR spectra of the un-doped and Sr(II) doped $LaFeO_3$ powders.

Similarly, for Co(II) doping, the absorption frequency of Fe-O stretching which is the characteristic absorption peak of $LaFeO_3$ structure was observed at about 590-620 cm^{-1} as shown in Figure 13. Moreover, when Co(II) increased, the weak bands around 1565 and 1440 cm^{-1} corresponding to the vibration of CO_3^{2-} group were also slightly noticed, especially in the case of LFCO50. According to this results, it could be assumed that large amounts of Sr(II) or Co(II) ions doping could interfere the formation of $LaFeO_3$ oxide. This assumption corresponded to the result of XRD which indicated that doping Sr(II) or Co(II) ions could restrain the grain growth of $LaFeO_3$.

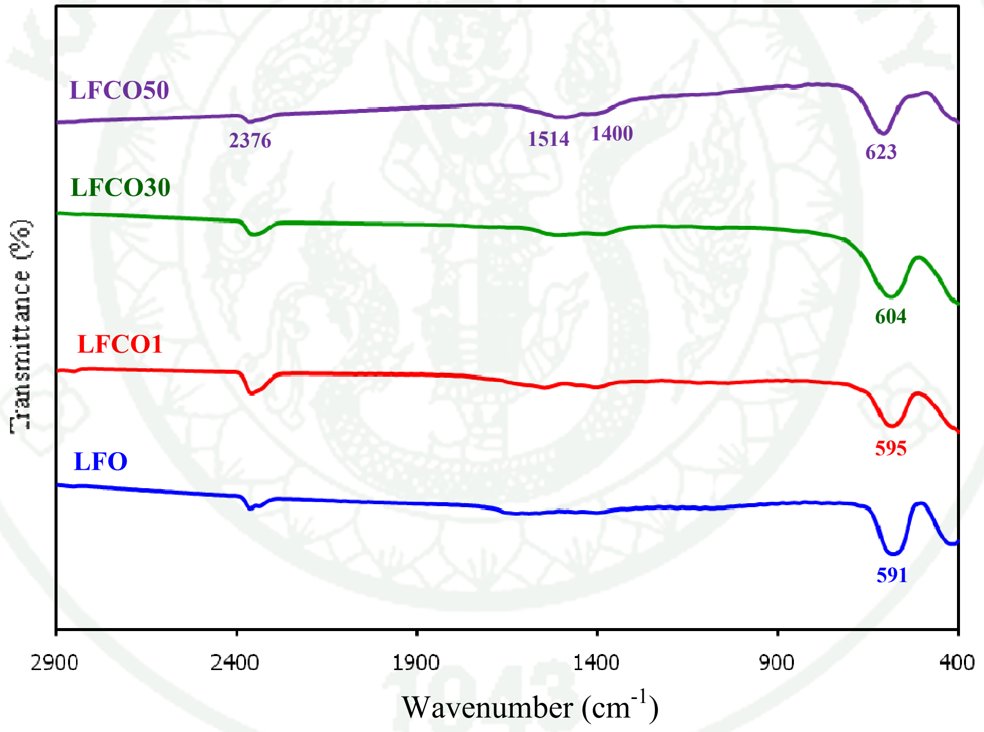

Figure 13 FTIR spectra of the un-doped and Co(II) doped $LaFeO_3$ powders.

Furthermore, in both of Sr(II) doped and Co(II) doped $LaFeO_3$ spectra, it is obviously seen that the characteristic absorption bands of Fe-O stretching gradully shifted to higher frequencies indicating that the bond strength, or may be referred to the bond length, of Fe-O was affected by the Sr(II) or Co(II) doped ions concentration. These results supported the XRD evidences which demonstrated that doping Sr(II) and Co(II) ions had an effect on the unit cell volume of $LaFeO_3$ by the formations of oxygen vacancies and Fe^{4+} ions resulting in the increasing of coulombic interaction between Fe^{4+} and O^{2-} and the decreasing of reduced mass in Fe-O bond (Barbero *et al.*, 2006). Thus, the results from XRD and FTIR could confirm that all of the prepared powders were $LaFeO_3$ perovskite, and both of Sr(II) and Co(II) ions used as a dopant could be doped into the structure of prepared $LaFeO_3$.

1.2.3 Scanning Electron Microscopy (SEM) and Energy Dispersive X-Ray Spectroscopy (EDS)

The results from SEM revealed that all of prepared powders exhibited similar surface morphologies of rather homogeneous microstructure. In particular, the images showed agglomeration of very small, fine particles with the porosity surface. The shape of these secondary aggregated particles was rather irregular and varied about 2-5 µm in size. However, because of the performance technique limitation, these SEM results could not reflect to the actual size of primary particles, but they could indicate that the prepared powders used further for films fabrication the films further were homogeneous and not quite different in size and shape. Figures 14-16 show SEM micrographs of the un-doped, Sr(II) doped and Co(II) doped $LaFeO_3$ powders with the magnification of 10000x.

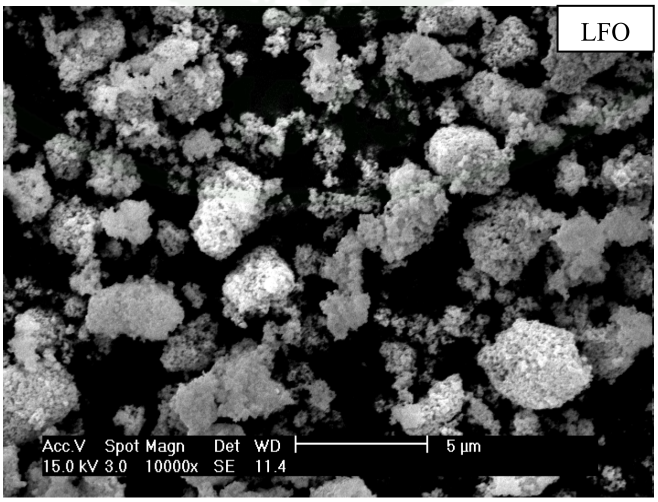

Figure 14 SEM micrograph of $LaFeO_3$ powder

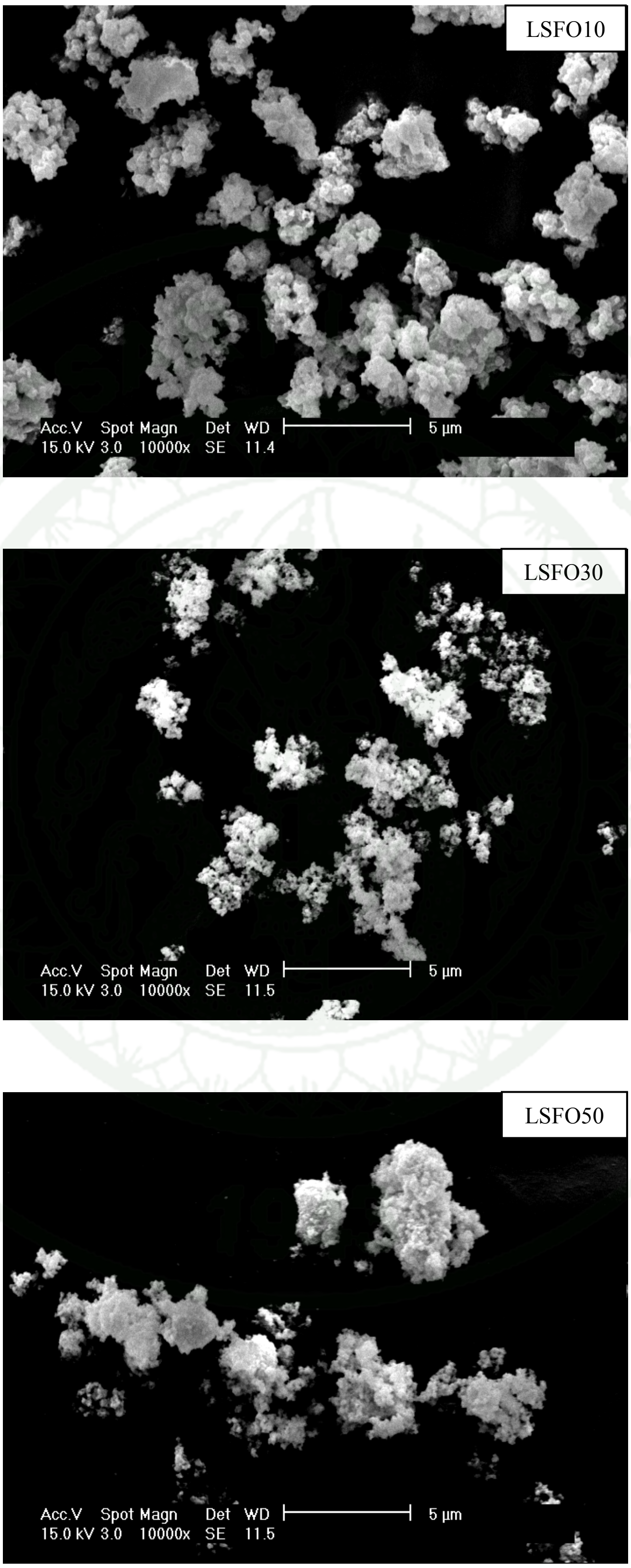

Figure 15 SEM micrographs of Sr(II) doped $LaFeO_3$ powders.

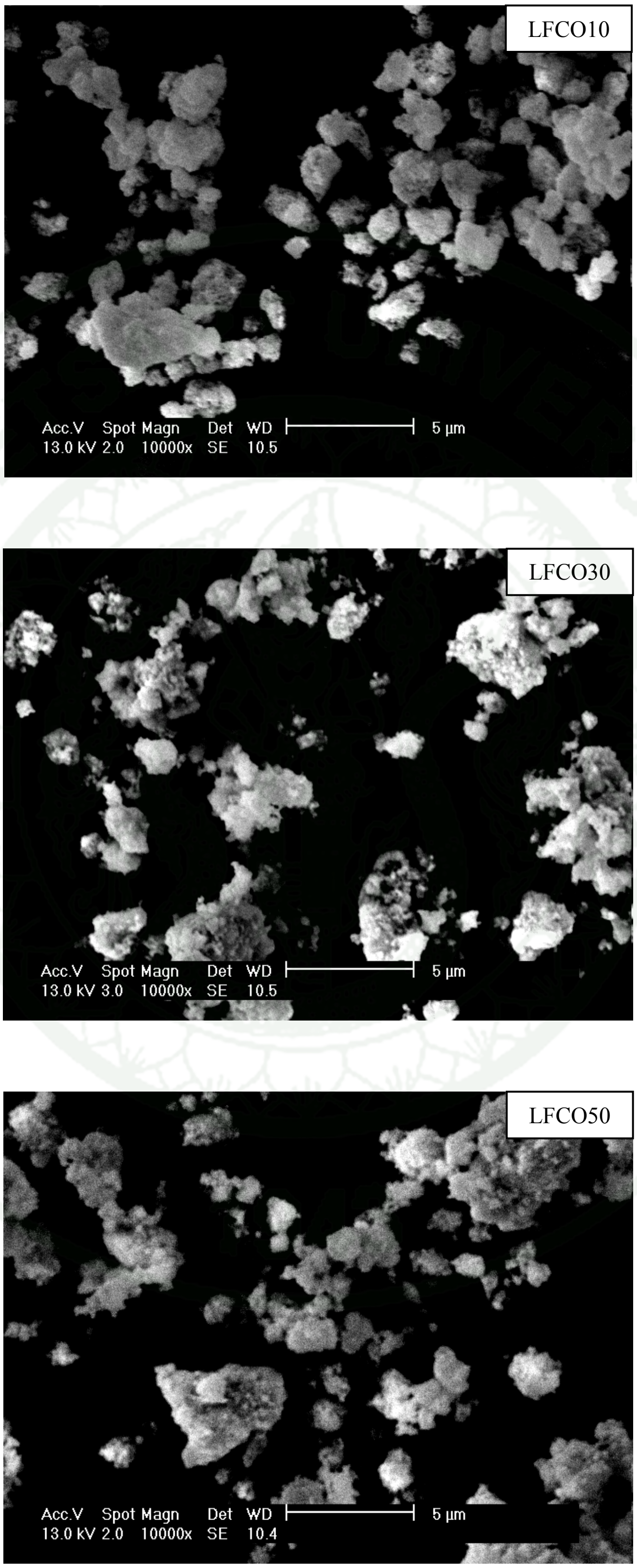

Figure 16 SEM micrographs of Co(II) doped $LaFeO_3$ powders.

Additionally, the elemental composition of prepared powders was performed by EDS in the scanning electron microscope. The EDS results in Table 9 and 10 show that the atomic ratio of Sr(II) and Co(II) had a tendency to increase when the amount of these doped ions increased. These results indicated that the Sr(II) or Co(II) used as dopants could be doped into prepared powders of $LaFeO_3$. Moreover, the results from EDX also supported the assumption of XRD results about the oxygen vacancies formation. Consider in the case of LFO, it can be seen that the atomic ratio of La: Fe: O was not exactly equal to the stoichiometric ratio of 1: 1: 3, in contrast, the relative ratio of O was lower than usual. This result supported the oxygen vacancies, and hence transformation of stoichiometric $LaFeO_3$ structure to a nonstoichiometric $LaFeO_{3-\delta}$ structure which usually found in the synthesis of $LaFeO_3$ at normal atmospheric condition (Delmastro *et al.*, 2001). So variation of the elemental composition in the experiment was observed.

Table 9 Elemental composition of the un-doped and Sr(II) doped $LaFeO_3$ powders

Perovskite oxide	Atomic ratio (%)							
	Experiment				Theory			
	La	Sr	Fe	O	La	Sr	Fe	O
LFO	27.57	-	25.71	46.72	20	-	20	60
LSFO10	27.59	2.21	21.55	48.65	18	2	20	60
LSFO30	26.77	9.13	18.33	45.76	14	6	20	60
LSFO50	10.75	13.63	20.49	55.13	10	10	20	60

Table 10 Elemental composition of the un-doped and Co(II) doped $LaFeO_3$ powders

Perovskite oxide	Atomic ratio (%)							
	Experiment				Theory			
	La	Fe	Co	O	La	Fe	Co	O
LFO	27.57	25.71	-	46.72	20	20	-	60
LFCO10	26.38	17.46	2.15	54.01	20	18	2	60
LFCO30	29.11	12.39	4.60	53.90	20	14	6	60
LFCO50	29.67	10.26	8.56	51.52	20	10	10	60

1.2.4 Brunauer, Emmett and Teller surface analysis (BET)

The results from BET analysis of all prepared powders illustrated slightly variable specific surface areas in the range of 7.88-12.45 m^2/g excepting in case of LFCO50 (Table 11). Moreover, it can be noticed that the powders of the highest doping amounts, which were LSFO50 and LFCO50, contained the largest surface area. This corresponded to the XRD results exhibiting that LSFO50 and LFCO50 powders had the lowest grain size values.

Table 11 Specific surface areas of the un-doped, Sr(II) doped and Co(II) doped $LaFeO_3$ powders

Perovskite oxide	Specific surface area (m^2/g)
LFO	11.41
LSFO10	7.88
LSFO30	10.18
LSFO50	12.45
LFCO10	11.04
LFCO30	8.84
LFCO50	18.99

2. Sensor fabrication

2.1 Characterization of $LaFeO_3$, Sr(II) doped $LaFeO_3$ and Co(II) doped $LaFeO_3$ sensors

2.1.1 Thermal Gravimetric Analysis (TGA)

After characterized by several essential techniques, the prepared powders were deposited on alumina substrates with gold electrodes to prepare sensors. In this process, the powders were ground into paste with triton X-100 binder and then coated on substrates by spin coating technique before annealed. Thus, the paste was characterized by TGA in order to determine an annealing temperature. The results shown in Figure 17 indicated the temperature of 500 ºC was appropriate to remove all organic contents because there is no weight loss was observed after this temperature.

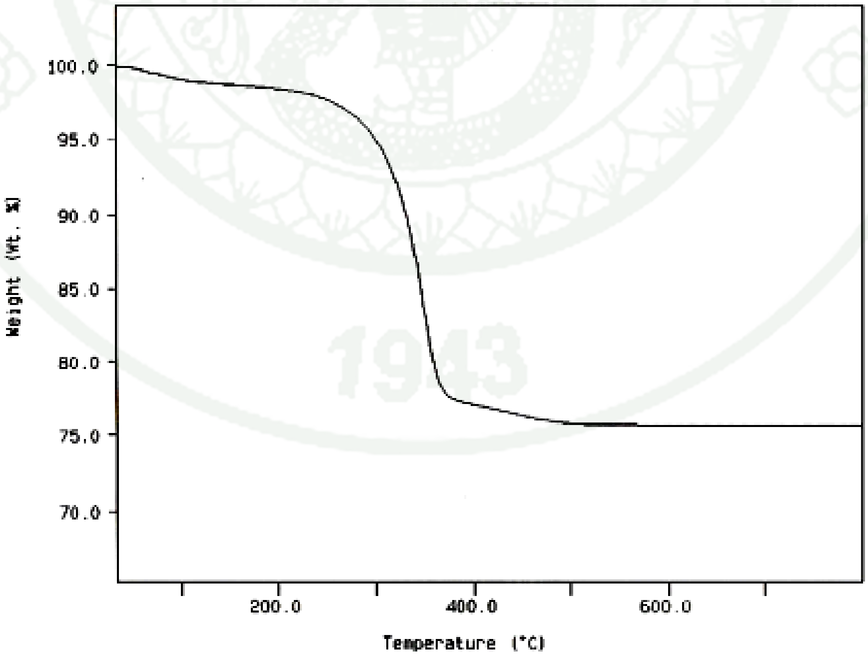

Figure 17 TGA thermogram of the paste ($LaFeO_3$, Triton X-100 and acetylacetone)

2.1.2 X-Ray Powder Diffraction (XRD)

XRD technique was used to confirm that the perovskite phase still remained in the oxide films sensors after annealed at 500 ºC for two hours. Figures 18 and 19 show the XRD patterns of the un-doped and Sr(II) doped and Co(II) doped $LaFeO_3$ sensors. The two highest peaks of $LaFeO_3$ (JCPDS file no. 37-1493) at the 2-theta about 32 and 57 ° in addition with many intense peaks of high crystallinity, alumina substrate; Al_2O_3 (JCPDS file no. 82-1467), and gold electrode; Au (JCPDS file no. 04-0784) were observed. This implied that all of sensors contained perovskite phase of $LaFeO_3$.

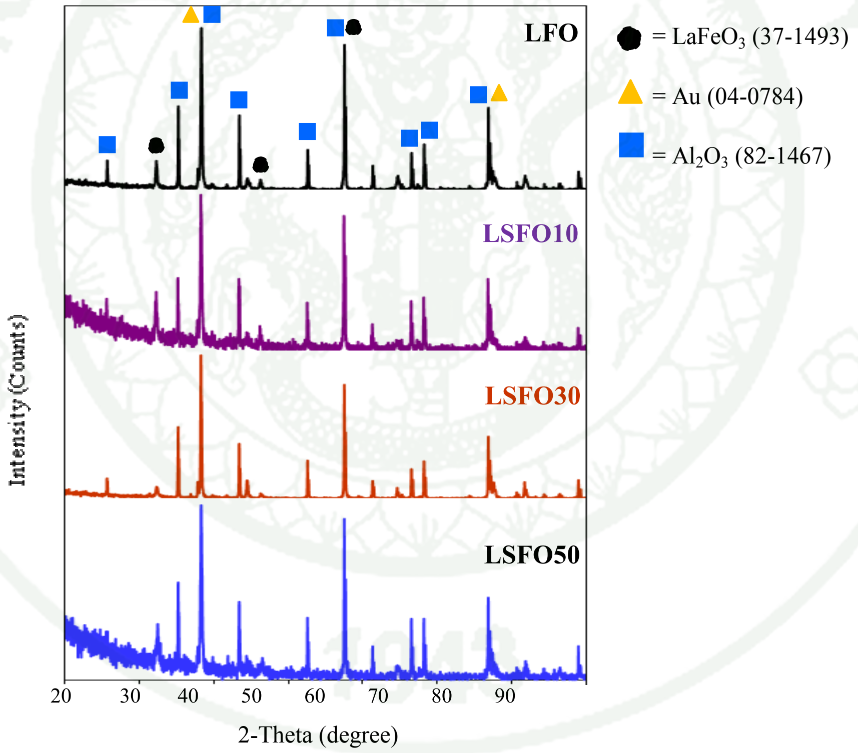

Figure 18 XRD patterns of the un-doped and Sr(II) doped $LaFeO_3$ sensors.

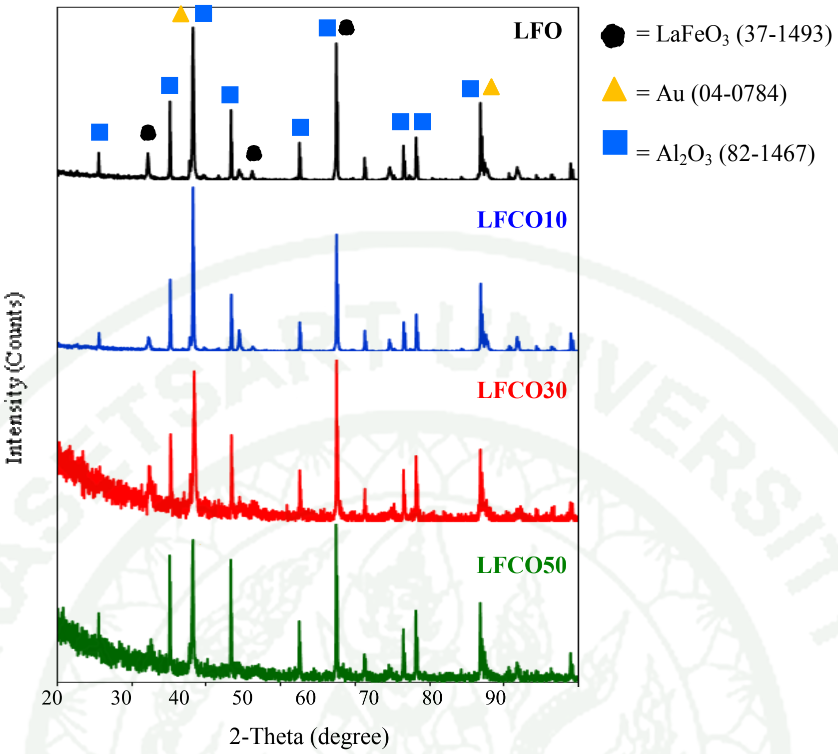

Figure 19 XRD patterns of the un-doped and Co(II) doped $LaFeO_3$ sensors.

2.1.3 Scanning electron microscopy (SEM)

The SEM micrographs of the un-doped, Sr(II) doped and Co(II) doped $LaFeO_3$ film sensors with the magnification of 5000x revealed rather similar surfaces of the oxide films as demonstrated in Figures 20-22. The film surfaces were homogeneous and continuous without cracking. In the case of Sr(II) doping, when the amounts of the dopant increased, the particles and porosity of the film surface is fine homogeneous and denser compared to the film with the same amount of Co(II) dopant.

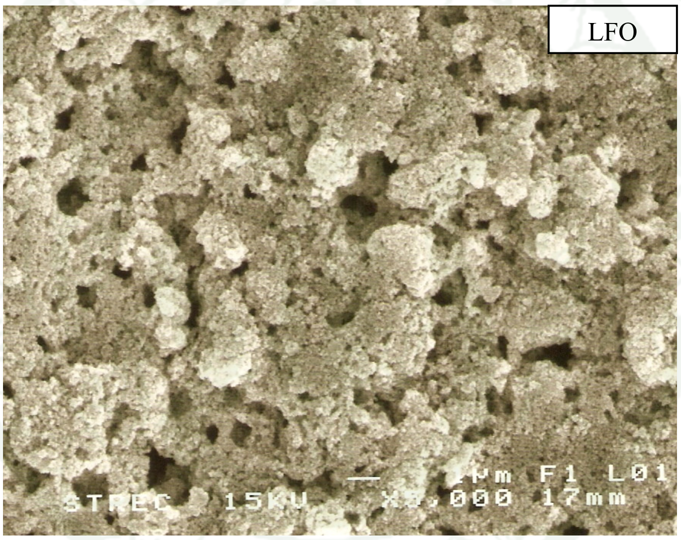

Figure 20 SEM micrograph of $LaFeO_3$ film sensor.

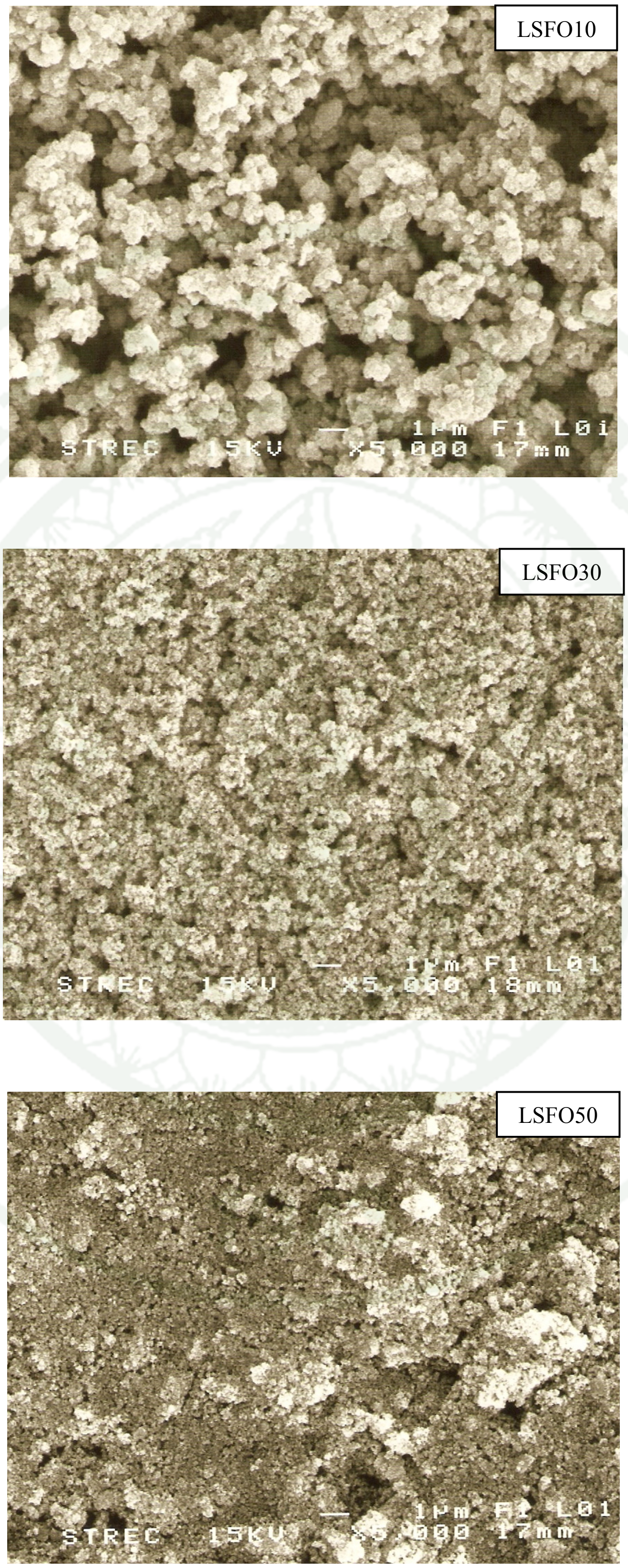

Figure 21 SEM micrographs of Sr(II) doped $LaFeO_3$ film sensors.

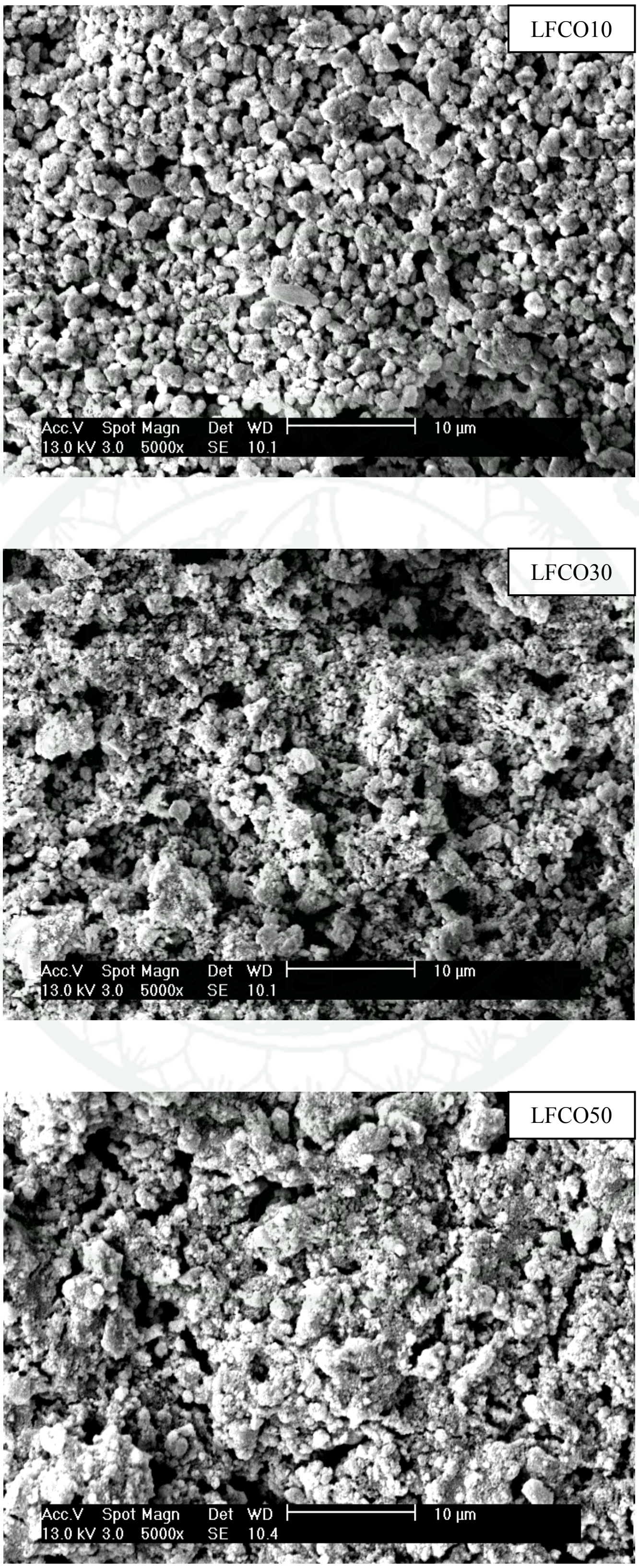

Figure 22 SEM micrographs of Co(II) doped $LaFeO_3$ film sensors.

2.1.4 Optical microscopy (OM)

The film thickness image of $LaFeO_3$ sensor perpendicularly fixed on a slide glass was estimated by an optical microscope with the magnification of 50x as demonstrated in Figure 23. All film thickness of prepared sensors was measured and found to approximately be 30-40 μm.

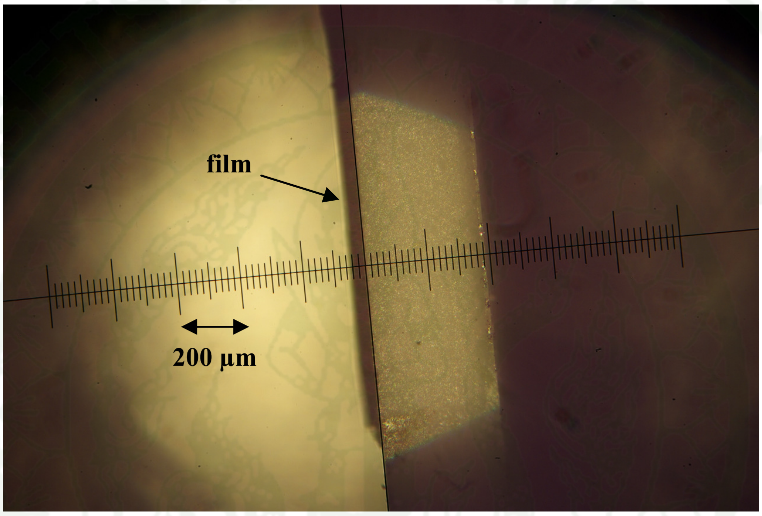

Figure 23 Film thickness image of $LaFeO_3$ sensor with the magnification of 50x.

2. Gas-sensing properties

2.1 Ethanol-sensing properties of Sr(II) doped and Co(II) doped $LaFeO_3$ sensors

For gas testing, the doped sensors were measured sensitivities simultaneously with the un-doped $LaFeO_3$ sensor in order to compare the effects of doping ions on sensing properties at the same condition. As the sensitivity of semiconductor gas sensor strongly depends on temperature. An optimal operating temperature of the prepared sensors was determined by measuring the responses to ethanol gas at various temperatures.

Figure 24 shows the responses of un-doped and Sr(II) doped $LaFeO_3$ sensors to 500 ppm ethanol gas at different temperatures. It can be seen that the responses of sensors slightly increased when the operating temperature increased to 350 °C. At this temperature, all of sensors exhibited the highest responses to ethanol gas, especially in the case of LSFO50. Thus in this work, the ethanol-sensing measurement of all Sr(II) doped $LaFeO_3$ sensors was performed at the temperature of 350 °C.

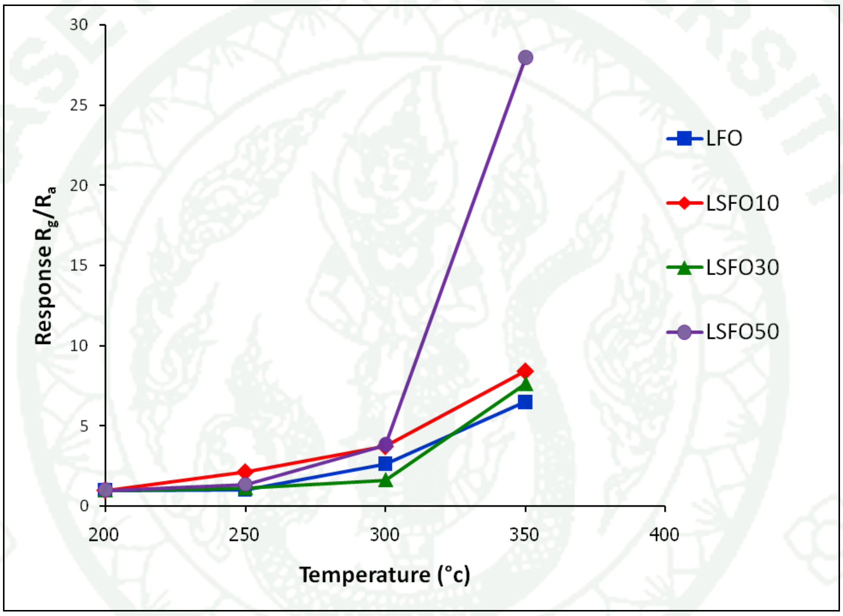

Figure 24 Responses to 500 ppm ethanol of un-doped and Sr(II) doped $LaFeO_3$ sensors operated at different temperatures.

The responses of un-doped and Sr(II) doped $LaFeO_3$ sensors to various concentrations of ethanol gas are presented in Figure 25 illustrating that LSFO50 sensor exhibited the highest response to various concentrations of ethanol gas. The response of LSFO50 sensor also significantly increased when the concentration of ethanol gas increased whereas the other sensors, such as LFO, LSFO10 and LSFO30, showed a little change in their responses. However, all of sensors seemed to reach the detection limit at 500 ppm because after this concentration, their responses were gradually increased. This might be due to insufficient active sites on the film surface of 2x3 mm sensors. If consider the relative response, defined by the ratio of responses of doped sensors and un-doped sensor, it is clearly seen that the LSFO50 sensor exhibited higher response to 500 ppm ethanol gas than LFO sensor about 4.29 times (Table 12). This indicated that the doping of 50% mole Sr(II) ions could improve the sensitivity to ethanol gas of prepared sensors. Furthermore, the response time, defined as the time to reach 90% at the final resistance (Wang *et al.*, 2008), of LSFO50 sensor was also improved. As illustrated in Table 12, it can be seen that the respond time to 500 ppm ethanol gas for LSFO50 sensor was only 120 seconds while the un-doped sensor was 210 seconds.

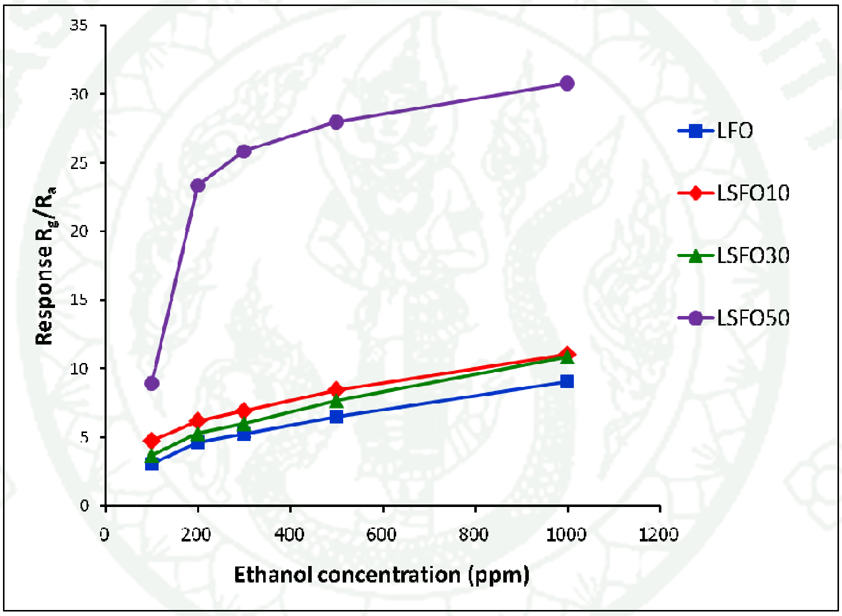

Figure 25 Responses to various ethanol gas concentrations of un-doped and Sr(II) doped $LaFeO_3$ sensors operated at 350 °C.

Table 12 Relative responses and response times to 500 ppm ethanol gas of un-doped and Sr(II) doped $LaFeO_3$ sensors operated at 350 °C

Sensor	Relative response	Response time (second)
LFO	1.00	210
LSFO10	1.29	180
LSFO30	1.18	250
LSFO50	4.29	120

For Co(II) doping, the responses to 500 ppm ethanol gas of Co(II) doped $LaFeO_3$ sensors were also measured at different temperatures to obtain the optimal operating temperature as the case of Sr(II) doping. The result in Figure 26 shows that all sensors exhibited the increasing response when operating temperature increased and gave the highest response at 350 °C which was the optimal temperature for ethanol-sensing of Co(II) doped $LaFeO_3$ sensors.

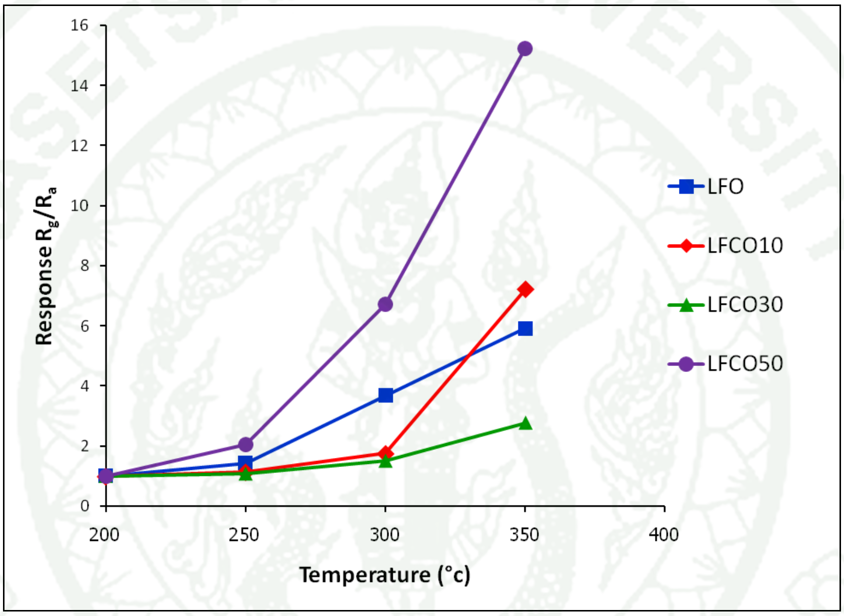

Figure 26 Responses to 500 ppm ethanol of un-doped and Co(II) doped $LaFeO_3$ sensors operated at different temperatures.

Figure 27 manifests the correlation between ethanol concentrations and responses of un-doped and Co(II) doped $LaFeO_3$ sensors at 350 °C. It can be seen that LFCO50 sensor exhibited the highest response to various concentrations of ethanol gas than other sensors. In addition, the response of LFCO50 sensor tremendously increased with the increasing of ethanol concentration but seemed to reach the maximum at 500 ppm. The next sensor that revealed moderate response to ethanol gas was LFO and LFCO10. The responses of these sensors were not much different and also slightly increased when the ethanol concentration increased to 500 ppm. Lastly, the sensor that had the lowest response was LFCO30 which showed a small change in response around 1 to 3 to various ethanol concentrations. Consider the relative response for comparing the responsibility between sensors to 500 ppm ethanol gas (Table 13), it can be seen that LFCO50 sensor could exhibit higher response than LFO sensor for 2.57 times. It suggested that the doping of Co(II) ions as 50% mole could improve the sensitivity to 500 ppm ethanol gas of $LaFeO_3$ sensor. Moreover, it was found that the time to respond ethanol gas of sensors could be improve by Co(II) doping as shown in Table 13 which illustrates that LFCO50 sensor could respond to 500 ppm of ethanol gas in 114 seconds, faster than those of the un-doped and other Co(II) doped sensors.

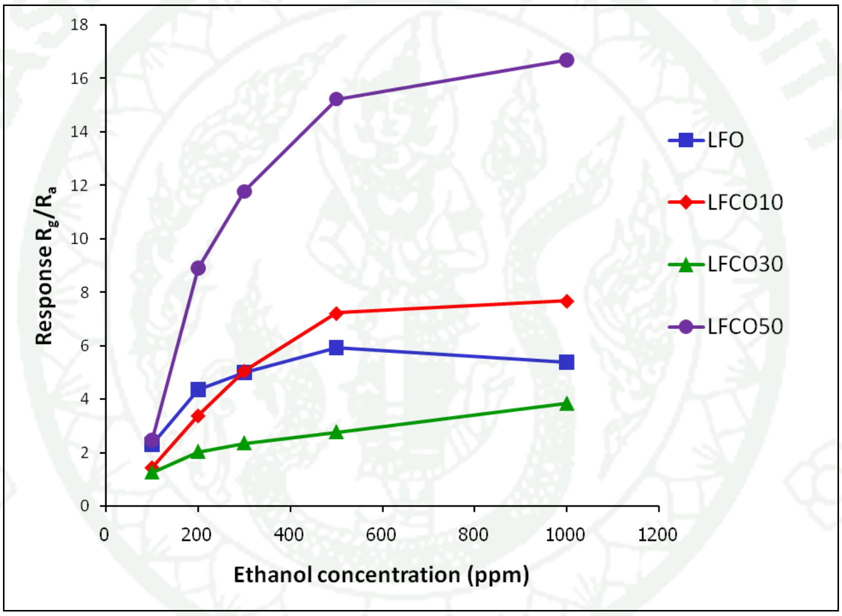

Figure 27 Responses to various ethanol gas concentrations of un-doped and Co(II) doped $LaFeO_3$ sensors operated at 350 °C.

Table 13 Relative responses and response times to 500 ppm ethanol gas of un-doped and Co(II) doped $LaFeO_3$ sensors operated at 350 °C

Sensor	Relative response	Response time (second)
LFO	1.00	222
LFCO10	1.22	204
LFCO30	0.47	150
LFCO50	2.57	114

2.2 Acetone-sensing properties of Sr(II) doped and Co(II) doped $LaFeO_3$ sensors

Figure 28 depicts the relationship between the operating temperature and the response of un-doped and Sr(II) doped $LaFeO_3$ sensors to 2000 ppm acetone gas. It is obvious that the response to acetone gas was strongly affected by the temperature and increased with the increasing temperature up to 350 °C which was appropriate for acetone-sensing of Sr(II) doped $LaFeO_3$ sensors.

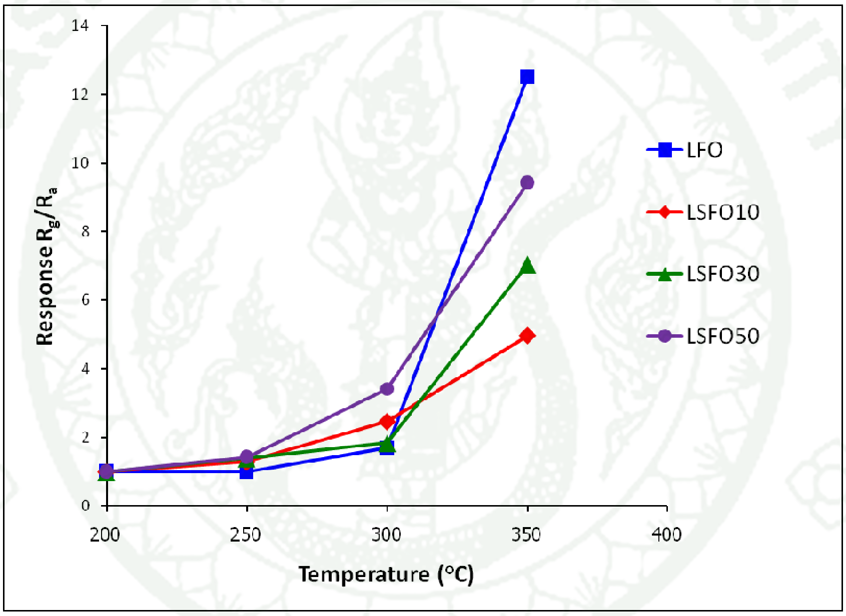

Figure 28 Responses to 2000 ppm acetone gas of un-doped and Sr(II) doped $LaFeO_3$ sensors operated at different temperatures.

The responses to various concentrations of acetone gas in Figured 29 illustrates that the un-doped $LaFeO_3$ sensor exhibited the highest response compared to those Sr(II) doped sensors. LFO sensor showed the increasing response with rather linearity whereas the LSFO50 exhibited the lower response in acetone concentrations of 200-2000 ppm. The lowest responses of LSFO30 and LSFO10 denoted poor responsibility, but however, their responses also increased with increasing of acetone concentrations. The relative responses and response times of all sensors to 2000 ppm acetone gas are summarized in Table 14.

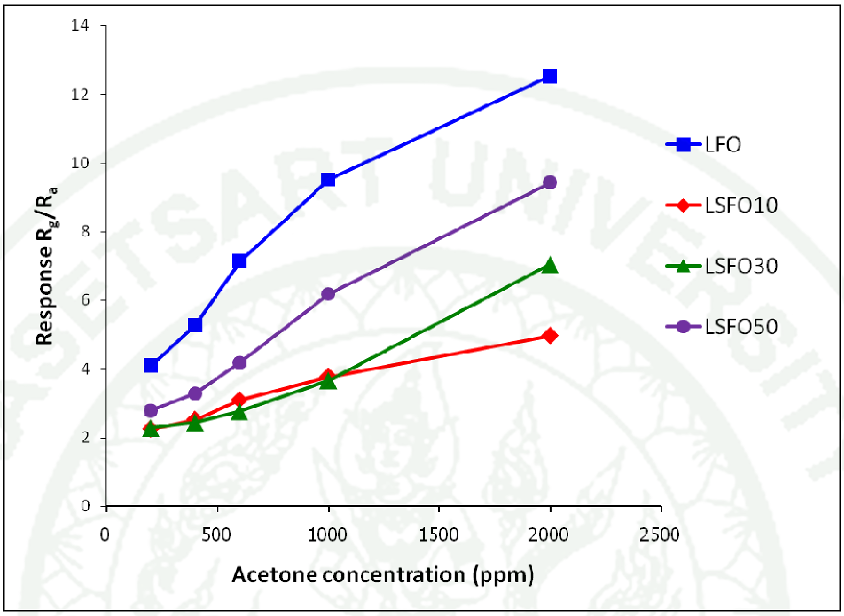

Figure 29 Responses to various acetone gas concentrations of un-doped and Sr(II) doped $LaFeO_3$ sensors operated at 350 °C.

Table 14 Relative responses and response times to 2000 ppm acetone gas of un-doped and Sr(II) doped $LaFeO_3$ sensors operated at 350 °C

Sensor	Relative response	Response time (second)
LFO	1.00	238
LSFO10	0.40	240
LSFO30	0.56	286
LSFO50	0.75	233

In the case of Co(II) doped, the responses to 2000 ppm acetone gas at different temperatures shown in Figure 30 indicated that all sensors were influenced by operating temperature and exhibited the highest response at 350 °C which was an appropriated temperature for acetone-sensing of all Co(II) doped sensors.

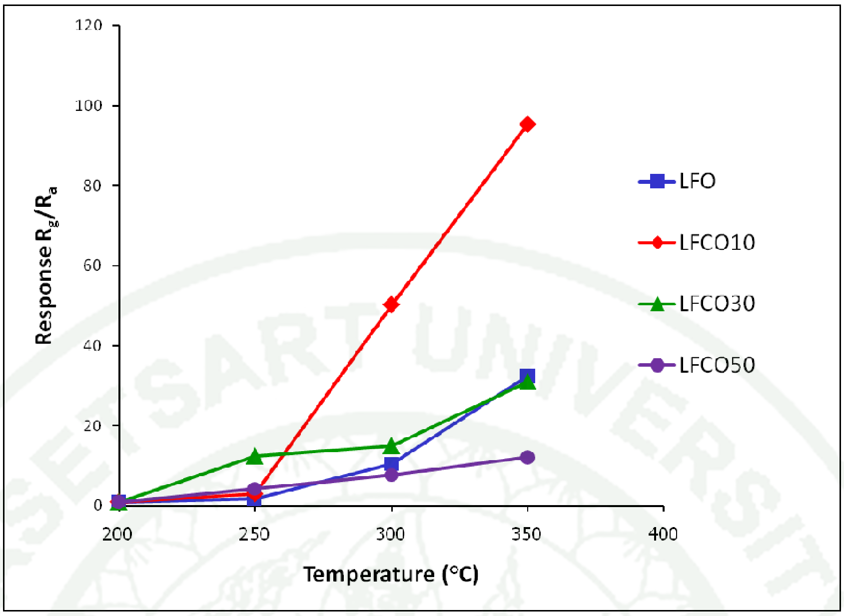

Figure 30 Responses to 2000 ppm acetone gas of un-doped and Co(II) doped $LaFeO_3$ sensors operated at different temperatures.

Figure 31 reveals the effect of acetone concentration on the responses of un-doped and Co(II) doped $LaFeO_3$ sensors at 350 °C. It is obviously seen that the LFCO10 sensor exhibited the highest response to various acetone concentrations while the other sensors showed a small change in their responses. Moreover, the reponse of LFCO10 sensor drastically increased with good linearity when the acetone concentration increased in the range of 200-2000 ppm. For comparing the responsibility to 2000 ppm acetone gas, it was found that the LFCO10 sensor exhibited higher response than the un-doped $LaFeO_3$ sensors about 2.94 times (Table 15). This indicated that the doping of 10% Co(II) could enhance the responsibility to acetone gas of $LaFeO_3$ sensor.

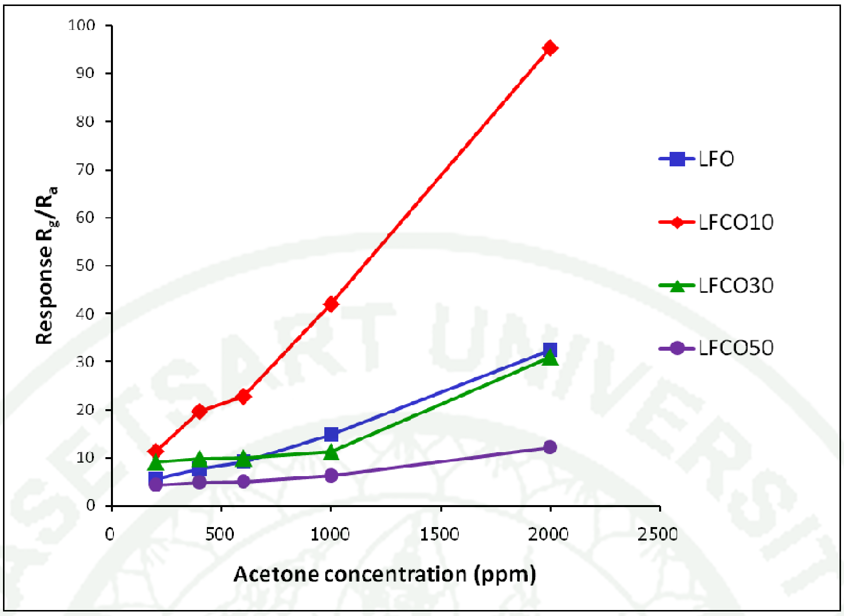

Figure 31 Responses to various acetone gas concentrations of un-doped and Co(II) doped LaFeO_3 sensors operated at 350 °C.

Table 15 Relative responses and response times to 2000 ppm acetone gas of un-doped and Co(II) doped LaFeO_3 sensors operated at 350 °C

Sensor	Relative response	Response time (second)
LFO	1.00	261
LFCO10	2.94	270
LFCO30	0.96	6
LFCO50	0.38	75

2.3 Sensing properties of Sr(II) doped and Co(II) doped LaFeO_3 sensors to other gases

The sensing properties of the other gases, such as, methane and hydrogen gases were also investigated. The results indicated that all of prepared sensors showed rather poor responsibility to these kinds of gases and exhibited very low response even the operating temperature raised up to 400 °C (Appendix G and H). The relative responses of all sensors to 20000 ppm methane gas at 400 °C and 30000 ppm hydrogen gas at 350 °C are summarized in Table 16.

Table 16 Relative responses of the un-doped, Sr(II) doped and Co(II) doped $LaFeO_3$ sensors to 20000 ppm methane gas at 400 °C and 30000 ppm hydrogen gas at 400 °C

Sensor	Relative response to methane gas	Relative response to hydrogen gas
LFO	1.00	1.00
LSFO10	0.86	0.89
LSFO30	1.34	1.49
LSFO50	2.04	1.38
LFCO10	0.93	1.71
LFCO30	0.43	1.27
LFCO50	0.38	1.33

2.4 The best sensor for ethanol and acetone gas

From the experiment, it was obvious that the LSFO50 was the promising sensor to detect the ethanol gas in the concentration range of 100-500 ppm at 350 °C with the resonably response and response time. Moreover, in spite of the high sensitivity, this sensor also exhibited rather good selectivity to ethanol gas. Figure 32 shows the responses of LSFO50 to various kinds of gases such as ethanol, acetone, methane and hydrogen at 350 °C. It is clearly seen that the sensor exhibited the high response to 500 ppm ethanol gas with the value of 27.97 whereas the 20000 ppm methane and 30000 ppm hydrogen gas were responded with the response only as 1.08 and 1.75, respectively.

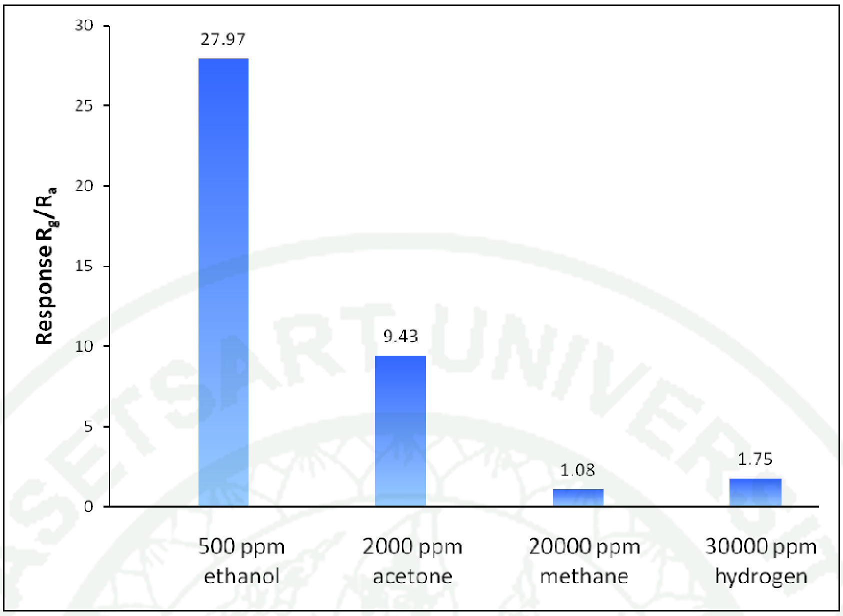

Figure 32 Responses of LSFO50 sensor to various kinds of gases operated at 350 °C

For acetone-sensing, the best sensitivity to acetone gas was observed in the case of LFCO10 sensor operated at 350 °C. This sensor showed the great response with the good linear relationship to 200-2000 ppm acetone gas. The sensor also exhibited the excellent selectivity to acetone gas at 350 °C when compared with the other gases such as ethanol, methane and hydrogen gas. Figure 33 reveals that the sensor exhibited very high response value of 95.38 to 2000 ppm acetone gas while the responses to 500 ppm ethanol, 50000 ppm methane and 30000 ppm hydrogen gas were determined as only 7.22, 2.24 and 2.25 respectively. These improving of acetone-sensing properties in LFCO10 sensor and ethanol-sensing properties of LSFO50 might be due to the effects of partial substitution of La^{3+} or Fe^{3+} by Sr^{2+} or Co^{2+} ions which caused the enhancing in active site such as oxygen vacancy and Fe^{4+} ion for catalytic reaction (Barbero *et al.*, 2006; Dai *et al.*, 2008)

.

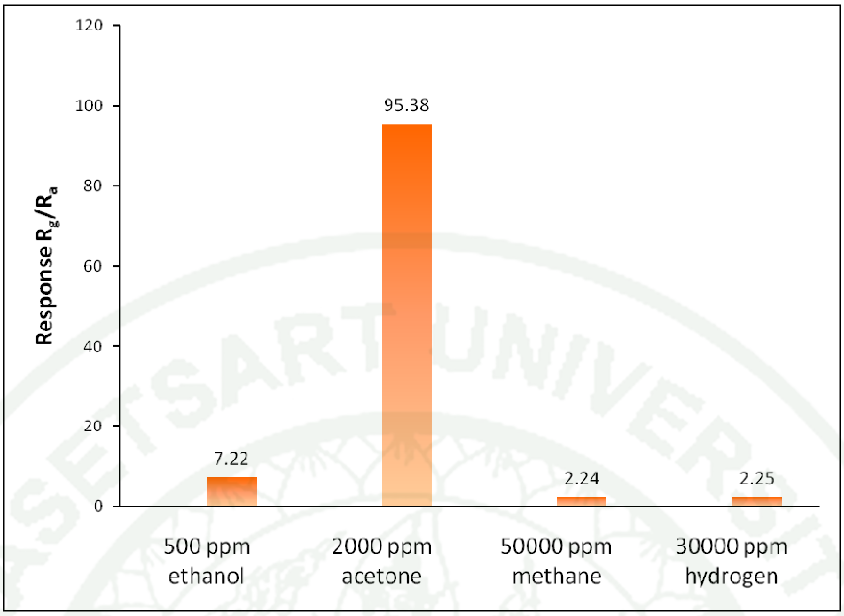

Figure 33 Responses of LFCO10 sensor to various kinds of gases operated at 350 °C

2.5 Gas-sensing mechanism

Figures 34 and 35 depict the sensing behavior to 500 ppm ethanol gas of LSFO50 sensors and the sensing characteristic of LFCO10 to 2000 ppm acetone gas operated at 350 °C which indicated that all of the un-doped, Sr(II) doped and Co(II) doped $LaFeO_3$ were p-type semiconductors (Chaudhari *et al.*, 2009). From the Figures, it can be seen that when the sensors were exposed in ethanol or acetone gas, their resistances were readily increased. This can be explained by the gas-surface interaction mechanism on the surface of semiconductors.

In general, when the sensor is heat up in air, the atmospheric oxygen is adsorbed on the transition metal ions of perovskite surface and the adsorbed oxygen molecules consume the valence electron from metal ions to become the chemisorbed oxygen as the following reactions (Liu *et al.*, 2008). This step results in depleting region of electron on semiconductor surface and the reduction of resistance in p-type material.

$$O_2\,(g) + e^- \longrightarrow O_2\,(ads) \qquad \text{------ (7)}$$

$$O_2\,(ads) + e^- \longrightarrow O_2^-\,(ads) \qquad \text{------ (8)}$$

$$O_2^-\,(ads) + e^- \longrightarrow 2O^-\,(ads) \qquad \text{------ (9)}$$

$$O^-\,(ads) + e^- \longrightarrow O^{2-}\,(ads) \qquad \text{------ (10)}$$

In the presence of a reducing gas such as ethanol or acetone, the reactions of adsorbed oxygen on the surface sensor with the gas occur as follow:

$$R + O^{n-}\,(ads) \longrightarrow RO + ne^- \qquad \text{------ (11)}$$

$$C_2H_5OH\,(g) + 6O^{n-}\,(ads) \longrightarrow 2CO_2 + 3H_2O + 6ne^- \qquad \text{------ (12)}$$

$$CH_3COCH_3 + 8O^{n-}\,(ads) \longrightarrow 3CO_2 + 3H_2O + 8ne^- \qquad \text{------ (13)}$$

$$H_2 + O^{n-}\,(ads) \longrightarrow H_2O + ne^- \qquad \text{------ (14)}$$

$$CH_4 + 4O^{n-}\,(ads) \longrightarrow CO_2 + 2H_2O + 4ne^- \qquad \text{------ (15)}$$

These electrons from the oxidation reactions is transported into material and recombine with holes (h•) in p-type semiconductor to maintain the neutrality.

$$h\bullet + e^- \longrightarrow \text{null} \qquad \text{------ (16)}$$

Since the hole carrier decreased, the conductance also decreased which consequently increased in resistance of the sensor as seen in the Figures.

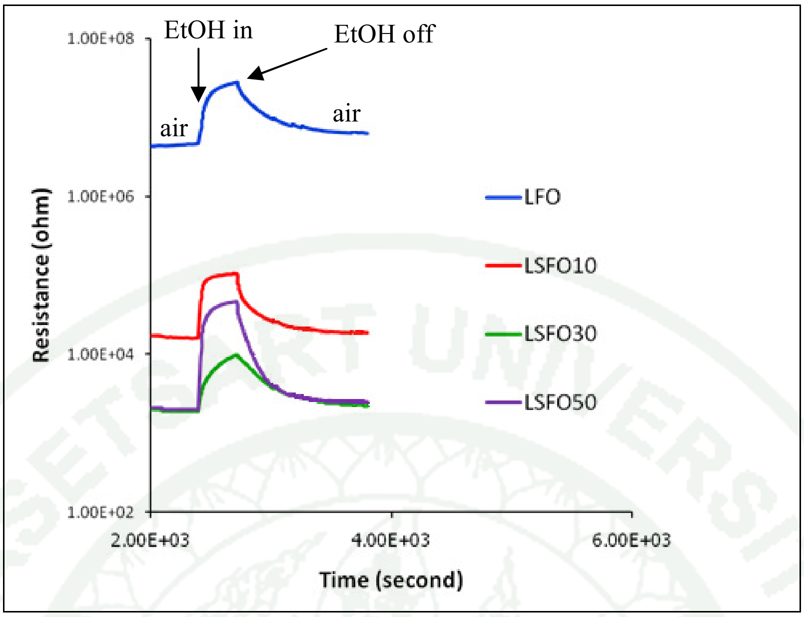

Figure 34 Response characteristics of Sr(II) doped $LaFeO_3$ sensors to 500 ppm ethanol gas operated at 350 °C.

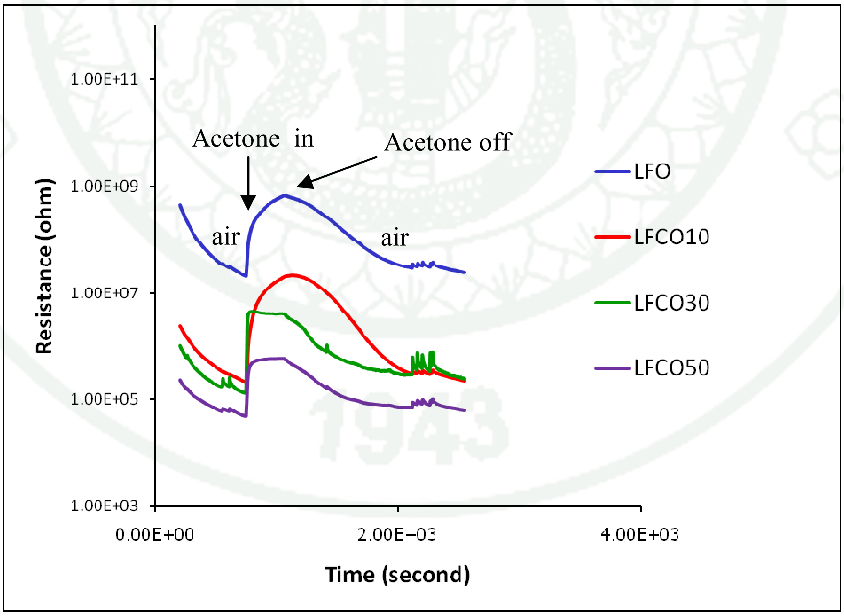

Figure 35 Response characteristics of Co(II) doped $LaFeO_3$ sensors to 2000 ppm acetone gas operated at 350 °C.

Sr(II) and Co(II) doping of $LaFeO_3$ do not affected only the sensitivity of the sensors, but also enhanced the conductivity of the sensor. All of Sr(II) and Co(II) doped sensors showed lower resistance comparing the un-doped sensor as illustrated in Figure 34 and 35. This result could be explained by the fact that when La^{3+} or Fe^{3+} ions in $LaFeO_3$ are substituted by the lower valency of Sr^{2+} or Co^{2+} ions, the hole carriers are generated because of the deficiency of valence electrons in the structure and results in the p-type characteristic of $LaFeO_3$ perovskite. The improving of conductivity and catalytic activity by partial substitution of La^{3+} or Fe^{3+} with the Sr^{2+} or Co^{2+} ions in $LaFeO_3$ structure might be contribute to the enhancing in gas-sensing properties of prepared sensors.

CONCLUSION

The un-doped, Sr(II) doped and Co(II) doped $LaFeO_3$ could be successfully synthesized by thermal decomposition of metal-organic complexes using triethanolamine as a ligand. The results from XRD and FTIR exhibited that all of prepared perovskite powders were orthorhombic structure of $LaFeO_3$ phase with the crystallite sizes around 14.31-41.71 nm. The unit cell volume and crystallite size of prepared powders were decreased when the amount of Sr(II) or Co(II) doping ions increased. The results from SEM and BET analysis revealed the small, fine particles of powders with average size of secondary aggregated particles about 2-5 μm and the specific surface area around 7.88-18.99 m^2/g.

Based on semiconducting properties, the gas-sensing properties of Sr(II) and Co(II) doped $LaFeO_3$ films prepared by spin coating were investigated. The results indicated that all of prepared perovskites were p-type semiconducting metal oxides. Doping of Sr(II) and Co(II) ions could improve the conductivity, sensitivity and selectivity of prepared sensors. At 350 °C operating temperature, the 50% Sr(II) doped sensor exhibited the highest response to 100-500 ppm ethanol gas with good selectivity when compared with acetone, methane and hydrogen gas while the sensors doped with 10% Co(II) showed the best response to 200-2000 ppm of acetone gas with very high selectivity. The improving of these sensing properties might be due to the enhancing of conductivity and catalytic activity by partial substitution of La^{3+} or Fe^{3+} with the Sr^{2+} or Co^{2+} ions.

LITERATURE CITED

Abdullah, M. and Khairurrijal. 2008. Derivation of scherrer equation using an approach in basic physics course. **J. Nano Saintek.** 1; 28-32.

Asada, T., T. Kayama, H. Kusaba, H. Einaga and Y. Teraoka. 2008. Preparation of alumina-supported $LaFeO_3$ catalysts and their catalytic activity for propane combustion. **Catal. Today.** 139: 37-42.

Barbero, B. P., J. A. Gamboa and L. E. Cardus. 2006. Synthesis and characterization of $La_{1-x}Ca_xFeO_3$ perovskite-type oxide catalysts for total oxidation of volatile organic compounds. **Appl. Catal., B.** 65: 21-30.

Berger, D., C. Matei, G. Voicu and A. Bobaru. 2010. Synthesis of $La_{1-x}Sr_xMO_3$ (M = Mo, Fe, Co, Ni) nanopowder by alanine-combustion technique. **J. Eur. Ceram. Soc.** 30: 617-622.

Bidrawn, F., G. Kim, N. Aramrueang, J. M. Vohs and R. J. Gorte. 2010. Dopants to enhance SOFC cathodes based on Sr-doped $LaFeO_3$ and $LaMnO_3$. **J. Power Sources.** 195: 720-728.

Biswas, S. K., A. Pathak, N. K. Pramanik, D. Dhak and P. Pramanik. 2008. Codoped Cr and W rutile nanosized powders obtained by pyrolysis of triethanolamine complexes. **Ceram. Int.** 34: 1875-1883.

Caronna, T., F. Fontana, I. N. Sora and R. Pelosato. 2009. Chemical synthesis and structural characterization of the substitution compound $LaFe_{1-x}Cu_xO_3$ (x = 0-0.40). **Mater. Chem. Phys.** 116: 645-648.

Dai, X., C. Yu and Q. Wu. 2008. Comparison of $LaFeO_3$, $La_{0.8}Sr_{0.2}FeO_3$ and , $La_{0.8}Sr_{0.2}Fe_{0.9}Co_{0.1}O_3$ perovskite oxides as oxygen carrier for partial oxidation of methane. **J. Nat. Gas Chem.** 17: 415-418.

Delmastro, A., D. Mazza, S. Ronchetti, M. Vallino, R. Spinicci, P. Brovetto and M. Salis. 2001. Synthesis and characterization of non-stoichiometric $LaFeO_3$ perovskite. **Mater. Sci. Eng. B.** 79: 140-145.

Farhadi, S., Z. Momeni and M. Taherimehr. 2009. Rapid synthesis of perovskite-type $LaFeO_3$ nanoparticles by microwave-assisted decomposition of bimetallic $La[Fe(CN)_6]$•$5H_2O$ compound. **J. Alloys Compd.** 471: L5-L8.

Gosavi, P. V. and R. B. Biniwale. 2010. Pure phase $LaFeO_3$ perovskite with improved surface area synthesized using different routes and its characterization. **Mater. Chem. Phys.** 119: 324-329.

Hammond, C. 2001. **The basics of crystallography and diffraction.** 2nd. Oxford University Press Inc. New York.

Haron, W. 2005. **Study on electrical property of $LaFeO_3$ doped with transition metal ions via one pot process.** Graduated School. Kasetsart University. Bankok.

Hueey, J.E., E. A. Keiter and R. L. Keiter. 1993. **Inorganic chemistry: principles of structure and reactivity.** 4th. HarperCollines College Publishers. New York.

Jadhav, A. D., A. B. Gaikawad, V. Samuel and V. Ravi. 2007. A low temperature route to prepare $LaFeO_3$ and $LaCoO_3$. **Mater. Lett.** 61: 2030-2032.

Karadag, A., V. T. Yilmaz, and C. Thoene. 2001. Di- and triethanolamine complexes of Co(II), Ni(II), Cu(II) and Zn(II) with thiocyanate: synthesis, spectral and thermal studies. Crystalstructure of dimeric Cu(II) complex with deprotonated diethanolamine, $[Cu_2(\mu\text{-dea})_2(NCS)_2]$. **Polyhedron.** 20: 635-641.

Kazak, C., S. Hamamci, Y. Topcu and V. T. Yilmaz. 2003. An eight-coordinate strontium complex with two tetradentate triethanolamine ligand: synthesis, IR spectra, thermal analysis and crystal structure of bis(triethanolamine)strontium(II). **J. Mol. Struct.** 657: 351-356.

Kong, L. and Y. Shen. 1996. Gas-sensing property and mechanism of $Ca_xLa_{1-x}FeO_3$ ceramics. **Sens. Actuators B.** 30: 217-221.

Korotcenkov, G. 2007. Metal oxides for solid-state gas sensor: What determines our choice?. **Mater. Sci. Eng., B.** 139: 1-23.

Leontiou, A. A., A. K. Ladavos, A. E. Giannakas, T. V. Bakas and P. J. Pomonis. 2007. A comparative study of substituted perovskite-type solids of oxidic $La_{1-x}Sr_xFeO_{3\pm\delta}$ and chlorinated $La_{1-x}Sr_xFeO_{3\pm\delta}Cl_\sigma$ form: Catalytic performance for CH_4 oxidation by O_2 or N_2O. **J. Catal.** 251: 103-112.

Li, F., H. Zheng, D. Jia, X. Xin and Z. Xue. 2002. Synthesis of perovskite-type composite oxides nanocrystals by solid-state reactions. **Mater. Lett.** 53: 282-286.

Li, S., L. Jing, W. Fu, L. Yang, B. Xin and H. Fu. 2007. Photoinduced charge property of nanosized perovskite-type $LaFeO_3$ and its relationships with photocatalytic activity under visible irradiation. **Mater. Res. Bull.** 42: 203-212.

Lima, R. K. C., M. S. Batista, M. Wallau, E. A. Sanches, Y.P. Mascarenhas and E. A. Urquieta-Gonza lez. 2009. High specific surface area LaFeCo perovskites-synthesis by nanocasting and catalytic behavior in the reduction of NO with CO. **Appl. Catal., B.** 90: 441-450.

Liou, Y. and Y. Chen. 2008. Synthesis and microstructure of (LaSr)MnO_3 and (LaSr)FeO_3 ceramics by a reaction-sintering process. **Ceram. Int.** 34: 273-278.

Liu, X., B. Cheng, J. Hu, H. Qin and M. Jiang. 2008. Semiconducting gas sensor for ethanol based on $LaMg_xFe_{1-x}O_3$ nanocrystals. **Sens. Actuators B.** 129: 53-58.

_______, H. Ji, Y. Gu and M. Xu. 2006. Preparation and acetone sensitive characteristics of nano-$LaFeO_3$ semiconductor thin films by polymerization complex method. **Mater. Sci. Eng. B.** 133; 98-101.

Nakamoto, K. 1997**. Infrared and raman spectra of inorganic and coordination compounds part B: applications in coordination, organometallic and bioinorganic chemistry.** 5th. John Wiley & Sons Inc. United State.

Popa, M., L. V. Hong and M. Kakihana. 2003. Nanopowders of $LaMeO_3$ perovskites obtained by a solution-based ceraic processing technique. **Phys. B.** 327:233-236.

Qi, X., J. Zhou, Z. Yue, Z. Gui and L. Li. 2003. A simple way to prepare nanosized $LaFeO_3$ powders at room temperature. **Ceram. Int.** 29: 347-349.

Shabbir, G., A. H. Qureshi and K. Saeed. 2006. Nano-crystalline $LaFeO_3$ powders synthesized by the citric-gel method. **Matter. Lett.** 60: 3706-3709.

Sogaard, M., P. V. Hendriksen and M. Mogensen. 2007. Oxygen nonstoichiometry and transport properties of strontium substituted lanthanum ferrite. **J. Solid state Chem.** 180: 1489-1503.

Song, P., H. Qin, L. Zhang, K. An, Z. Lin, J. Hu and M. Jiang. 2005. The structure, electrical and ethanol-sensing properties of $La_{1-x}Pb_xFeO_3$ perovskite ceramics with $x \leq 0.3$. **Sens. Actuators B.** 104: 312-316.

_______, H. Qin, X. Liu, S. Huang, R. Zhang, J. Hu and M. Jiang. 2006. Structure, electrical and CO-sensing properties of the $La_{0.8}Pb_{0.2}Fe_{1-x}Co_xO_3$ system, **Sens. Actuators B.** 119: 415–418.

_______, Q. Wang and Z. Yang. 2009. The effects of annealing temperature on the CO-sensing property of perovskite $La_{0.8}Pb_{0.2}Fe_{0.8}Cu_{0.2}O_3$ nanoparticles. **Sens. Actuators B.** 141: 109-115.

Sunarso, J., S. Baumann, J. M. Serra, W. A. Meulenberg, S. Liu, Y. S. Lin, J. C. Diniz da Costa. 2008. Mixed ionic-electronic conducting (MIEC) ceramic-based membranes for oxygen separation. **J. Membr. Sci.** 320: 13-41.

Tanaka, H. and M. Misono. 2001. Advances in designing perovskite catalysts. **Curr. Opin. Solid St. M.** 5: 381-387.

Toan, N.N., S. Saukko and V. Lantto. 2003. Gas sensing with semiconducting perovskite oxide $LaFeO_3$. **Phys. B.** 327: 279-282.

Traversa, E., P. Nunziantel, M. Sakamoto, Y. Sadaoka and R. Montanari. 1998. Synthesis and structural characterization of trimetallic perovskite-type oxides, $LaFe_xCo_{1-x}O_3$, by the themal decomposition of cyano complexes, $La[Fe_xCo_{1-x}(CN)_6]\bullet nH_2O$. **Matter. Res. Bull.** 33: 673-681.

Wang, Y., J. Zhu, L. Xujie, Y. Lude and X. Wang. 2006. Preparation and characterization of perovskite $LaFeO_3$ nanocrystals. **Mater. Lett.** 60: 1767-1770.

Wang, Y. Wang, J. Cao, F. Kong, H. Xia, J. Zhang, B. Zhu, S. Wang and S. Wu. 2008. Low-temperature H_2S sensors based on Ag doped α-Fe_2O_3 nanoparticles. **Sens. Actuators B.** 131: 183-189.

Warnhus, I., N. Sakai, H. Yokokawa, T. Grande, M. Einarsrud and K. Wiik. 2004. Mass transport in $La_{1-x}Sr_xFeO_3$ ($x = 0$ and 0.1) measured by SIMS. **Solid State Ionics.** 175: 69-71.

Wei, Z. Y. Xu, H. Liu and C. Hu. 2009. Preparation and catalytic activities of $LaFeO_3$ and Fe_2O_3 for HMX thermal decomposition. **J. Hazard. Mater.** 165: 1056-1061.

Xiangfeng, C. and P. Siciliano. 2003. CH_3SH-sensing characteristics of $LaFeO_3$ thick-film prepared by co-precipitation method. **Sens. Actuators B.** 94: 197-200.

Xing, L., B. Cheng, J. Hu, H. Qin and M. Jiang. 2008. Semiconducting gas sensor for ethanol based on $LaMg_xFe_{1-x}O_3$ nanocrystals. **Sens. Actuators, B.** 129: 53-58.

Yang, M., A. Xu, H. Du, C. Sun and C. Li. 2007. Removal of salicylic acid on perovskite-type oxide $LaFeO_3$ catalyst in catalytic wet air oxidation process. **J. Hazard. Mater. B.** 139: 86-92.

Zheng, W., R. Liu, D. Peng and G. Meng. 2000. Hydrothermal synthesis of $LaFeO_3$ under carbonate-containing medium. **Mater. Lett.** 43: 19-22.

APPENDICES

Appendix A

TGA thermograms of metal-organic complex precursors

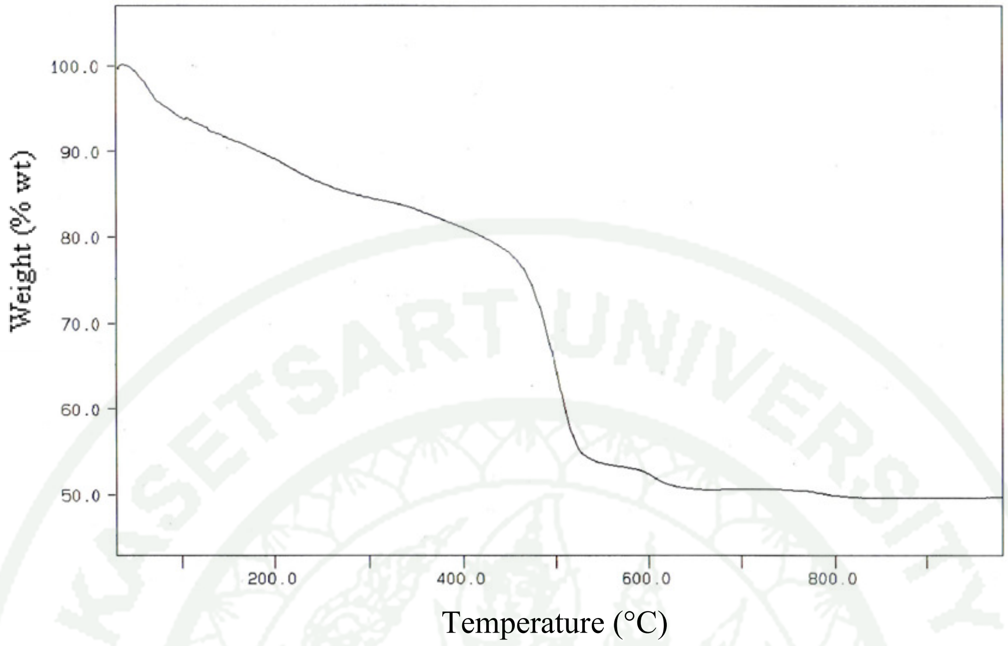

Appendix Figure A1 TGA thermogram of LSFO10 precursor.

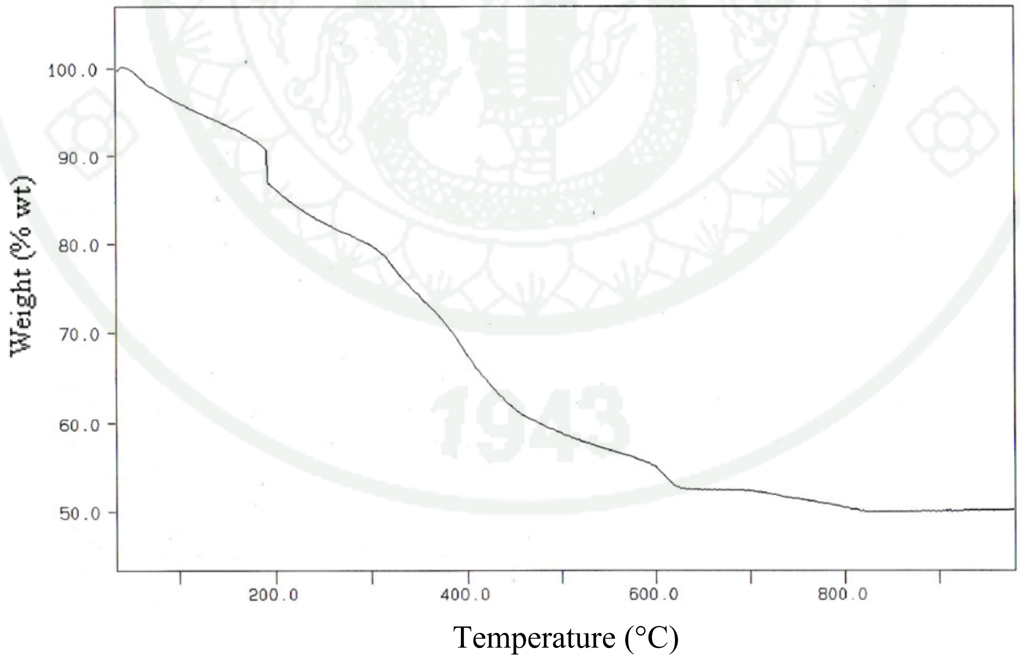

Appendix Figure A2 TGA thermogram of LSFO30 precursor.

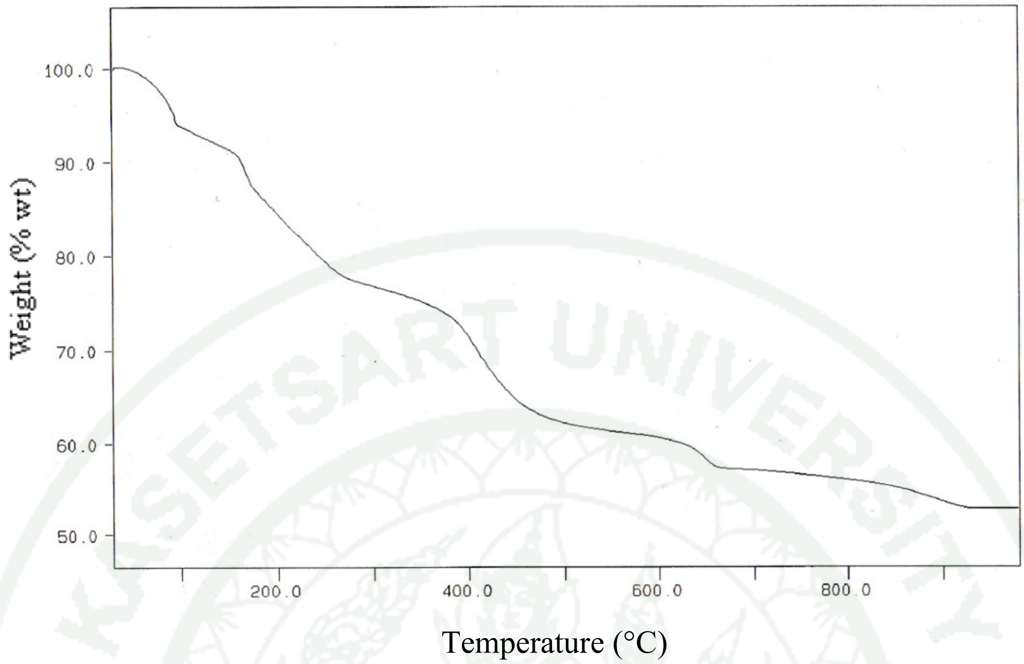

Appendix Figure A3 TGA thermogram of LSFO50 precursor.

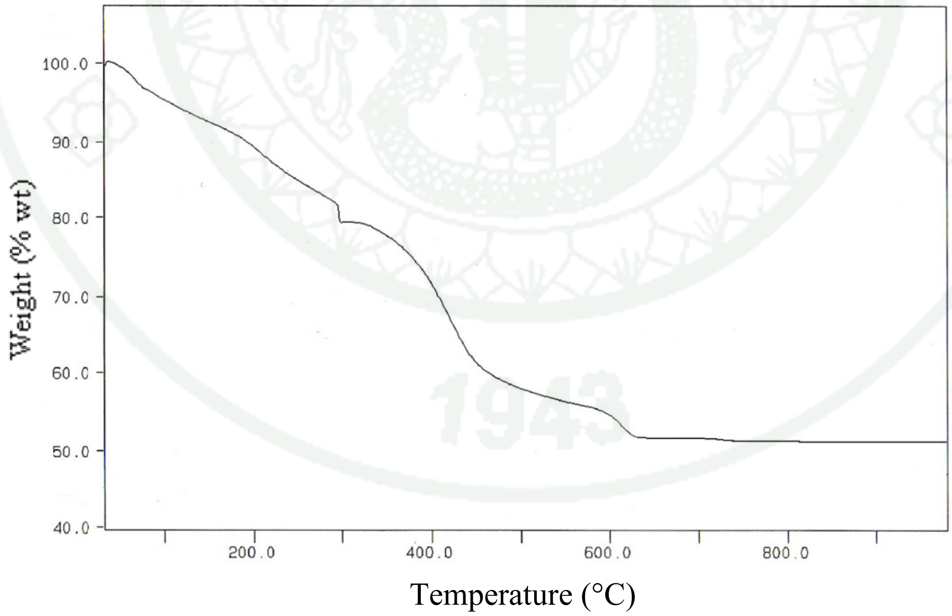

Appendix Figure A4 TGA thermogram of LFCO10 precursor.

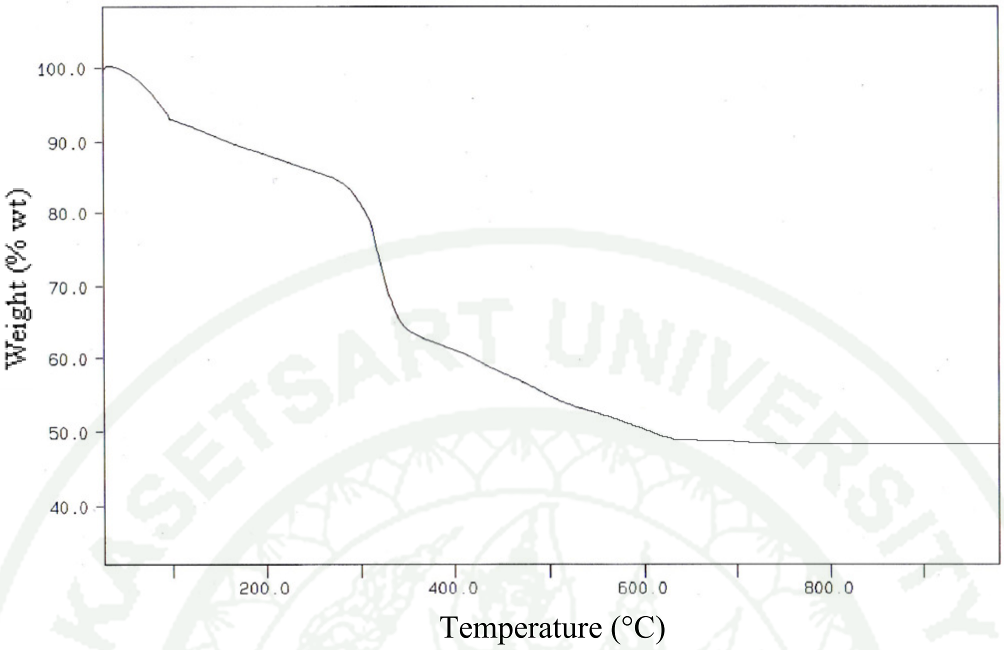

Appendix Figure A5 TGA thermogram of LFCO30 precursor.

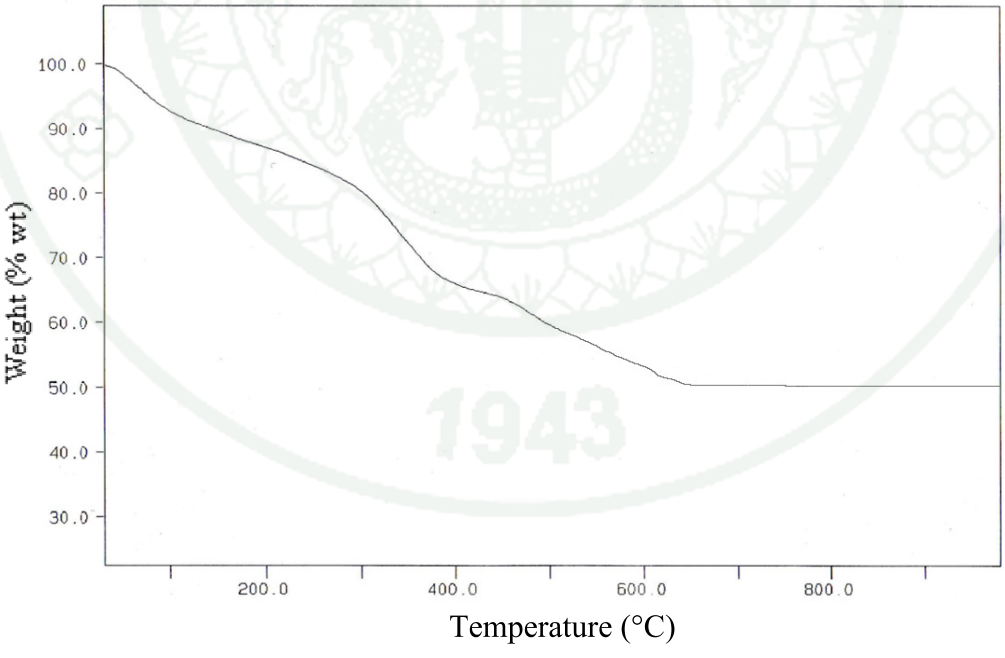

Appendix Figure A6 TGA thermogram of LFCO50 precursor.

Appendix B

FTIR spectra of metal-organic complex precursors

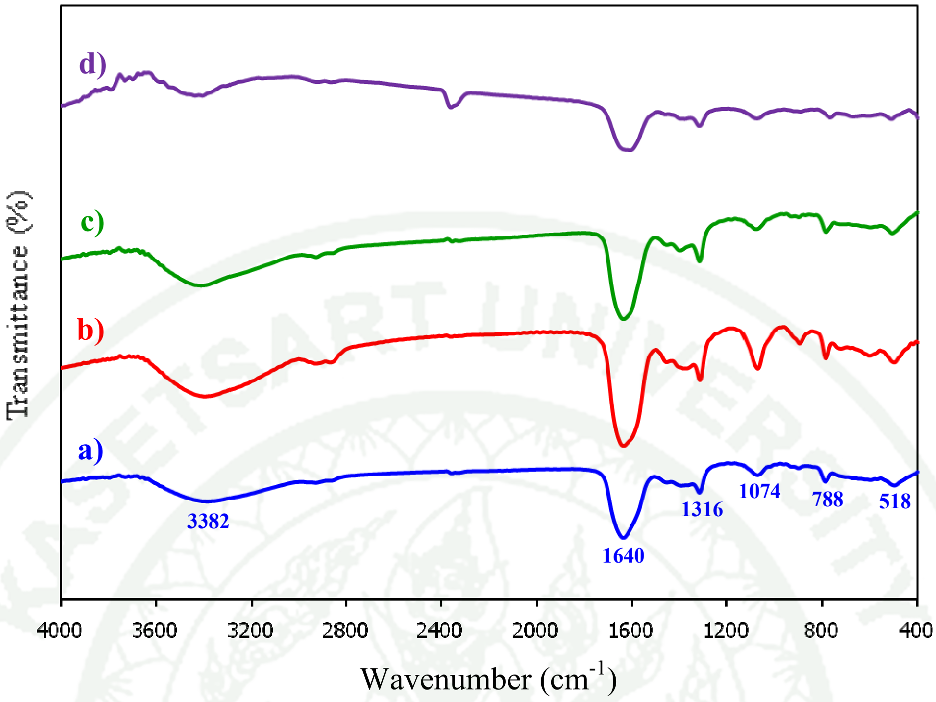

Appendix Figure B1 FTIR spectra of a) LFO b) LSFO10 c) LSFO30 and d) LSFO50 precursors.

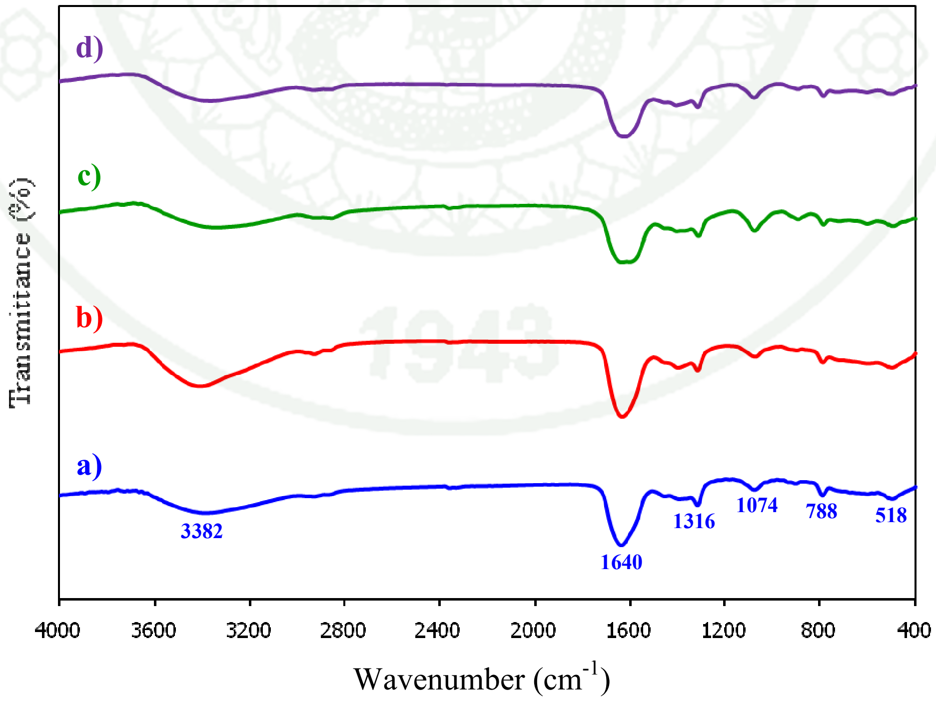

Appendix Figure B2 FTIR spectra of a) LFO b)LFCO10 c) LFCO30 and d) LFCO50 precursors.

Appendix C

Calculation of crystallite size by Scherrer equation

The crystallite sizes of prepared powders were calculated using Scherrer equation as shown in equation (5) (see section 1.4.1 in material and method, p. 27). The size of crystals is determined by the width of the strongest diffraction peak in XRD pattern. The FWHM of the selected diffraction peak was estimated by using a fityk program, free software for nonlinear fitting method, to fit the diffraction profile with a Lorentzian function (Abdullah and Khairurrijal, 2008). Appendix Figure C1 shows the example of the peak fitting of (121) plane from the LFO data which provides the important parameters such as the location and the width of the peak. Since the values of λ and K were 0.1542495 and 0.9, respectively, the crystallite size of LFO powder was calculated as:

$$t = \frac{0.1542495\ (nm)\ X\ 0.9}{0.003449\ (rad)\ X \cos(32.221/2)} = 41.892\ nm$$

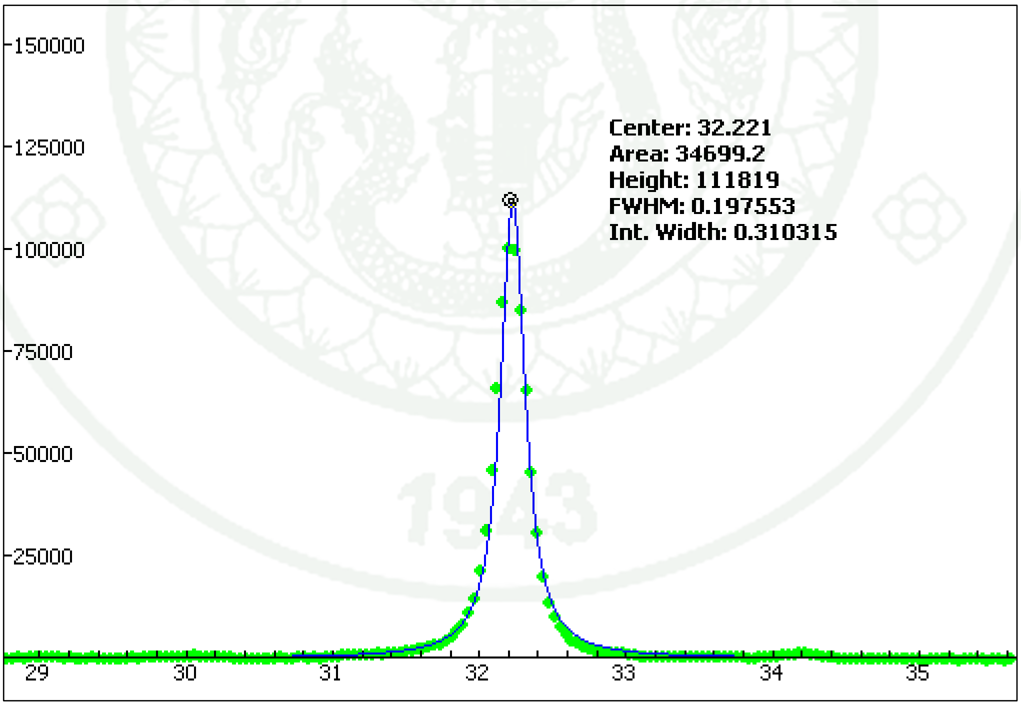

Appendix Figure C1 Peak fitting with a Lorentzian function at 2θ of 32.221°.

Appendix D

Calculation of lattice parameters

Lattice parameters of the unit cell were calculated by the relationship of an orthorhombic system as shown in equation (3) (see section 1.4.1 in material and method, p. 27). The d-spacing used in this equation is acquired from Bragg's law given by:

$$2d\sin\theta = n\lambda \qquad \text{------ (17)}$$

where θ is a Bragg's angle

n is an order of reflection (integer; n = 1)

λ is the wavelength of an X-ray source (CuKα; λ = 0.154 nm)

In experiment, the d-spacing values were calculated from three main diffraction peaks of (121), (240) and (202) planes (Table 6). According to equation (3), the correlation between d-spacing values, Miller indices and lattice parameters of LFO powder are written by:

(121) plane; $$\frac{1}{2.7828^2} = \frac{1}{a^2} + \frac{2^2}{b^2} + \frac{1}{c^2} \qquad \text{------ (18)}$$

(240) plane; $$\frac{1}{1.6069^2} = \frac{2^2}{a^2} + \frac{4^2}{b^2} \qquad \text{------ (19)}$$

(202) plane; $$\frac{1}{1.9679^2} = \frac{2^2}{a^2} + \frac{2^2}{c^2} \qquad \text{------ (20)}$$

For finding a, b and c parameters, the equations (18), (19) and (20) were solved together and gave the result as; a = 5.5692 Å, b = 7.8702 Å and c = 5.5628 Å. Thus, the unit cell volumn of prepared LFO powder was determined as (5.5692 x 7.8702 x 5.5628) = 243.82 Å^3.

Appendix E

Ethanol-sensing data of the un-doped, Sr(II) doped and Co(II) doped $LaFeO_3$ sensors

Appendix Table E1 Responses to 500 ppm ethanol gas of un-doped, Sr(II) doped and Co(II) doped $LaFeO_3$ sensors operated at different temperatures

Perovskite	Operating temperature (°C)			
sensor	200	250	300	350
LFO	1.00	1.05	2.67	6.52
LSFO10	1.00	2.14	3.74	8.42
LSFO30	1.00	1.15	1.65	7.67
LSFO50	1.00	1.36	3.84	27.97
LFO	1.00	1.43	3.68	5.92
LFCO10	1.00	1.14	1.76	7.22
LFCO30	1.00	1.08	1.51	2.78
LFCO50	1.00	2.06	6.73	15.24

Appendix Table E2 Responses to various ethanol gas concentrations of un-doped, Sr(II) doped and Co(II) doped $LaFeO_3$ sensors operated at 350 °C

Perovskite	Ethanol gas concentrations (ppm)				
sensor	100	200	300	500	1000
LFO	3.07	4.64	5.26	6.52	9.06
LSFO10	4.73	6.18	6.90	8.42	11.01
LSFO30	3.67	5.26	6.00	7.67	10.85
LSFO50	8.92	23.35	25.84	27.97	30.79
LFO	2.30	4.35	4.99	5.92	5.37
LFCO10	1.44	3.39	5.06	7.22	7.68
LFCO30	1.27	2.04	2.36	2.78	3.84
LFCO50	2.48	8.92	11.79	15.24	16.70

Appendix F

Acetone-sensing data of the un-doped, Sr(II) doped and Co(II) doped $LaFeO_3$

Appendix Table F1 Responses to 2000 ppm acetone gas of un-doped, Sr(II) doped and Co(II) doped $LaFeO_3$ sensors operated at different temperatures

Perovskite	Operating temperature (°C)			
sensor	200	250	300	350
LFO	1.00	1.00	1.69	12.52
LSFO10	1.00	1.29	2.46	4.96
LSFO30	1.00	1.40	1.84	7.05
LSFO50	1.00	1.42	3.41	9.43
LFO	1.00	1.89	10.55	32.46
LFCO10	1.00	3.06	50.31	95.38
LFCO30	1.00	12.53	15.09	31.04
LFCO50	1.00	4.37	7.74	12.20

Appendix Table F2 Responses to various acetone gas concentrations of un-doped, Sr(II) doped and Co(II) doped $LaFeO_3$ sensors operated at 350 °C

Perovskite	Acetone gas concentrations (ppm)				
sensor	200	400	600	1000	2000
LFO	4.10	5.28	7.13	9.52	12.52
LSFO10	2.26	2.53	3.10	3.78	4.96
LSFO30	2.29	2.46	2.77	3.67	7.05
LSFO50	2.79	3.30	4.18	6.18	9.43
LFO	5.59	7.79	9.17	14.80	32.46
LFCO10	11.28	19.65	22.75	42.00	95.38
LFCO30	9.17	9.96	9.98	11.30	31.04
LFCO50	4.36	4.92	5.08	6.33	12.20

Appendix G

Methane-sensing data of the un-doped, Sr(II) doped and Co(II) doped $LaFeO_3$

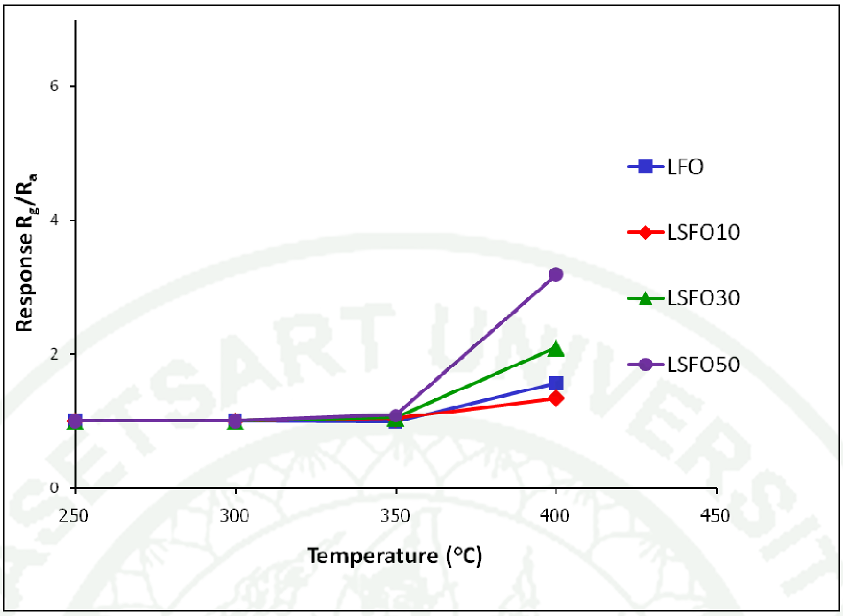

Appendix Figure G1 Responses to 20000 ppm methane gas of un-doped and Sr(II) doped $LaFeO_3$ sensors operated at different temperatures.

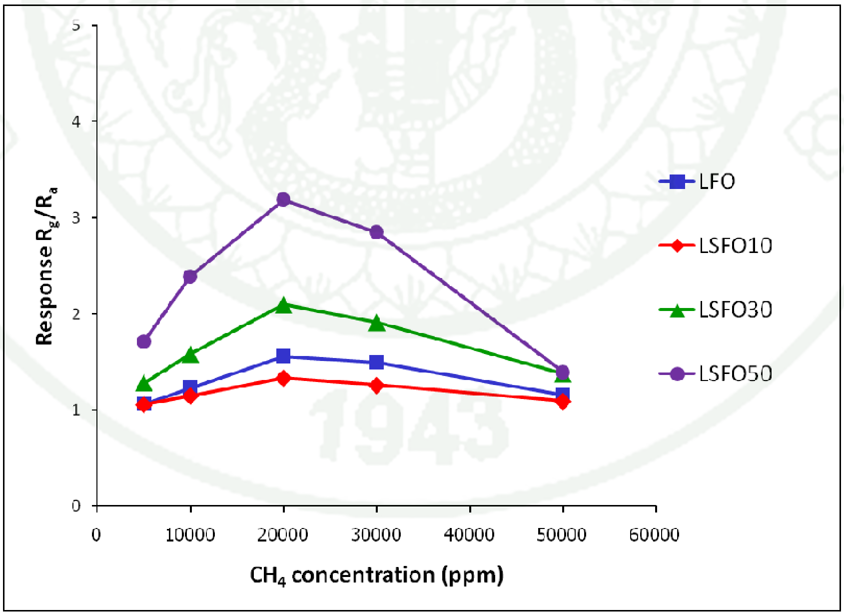

Appendix Figure G2 Responses to various methane gas concentrations of un-doped and Sr(II) doped $LaFeO_3$ sensors operated at 400 °C.

Appendix Table G1 Responses to 20000 ppm methane gas of un-doped and Sr(II) doped $LaFeO_3$ sensors operated at different temperatures

Perovskite sensor	Operating temperature (°C)			
	250	300	350	400
LFO	1.00	1.00	0.98	1.56
LSFO10	1.00	1.00	1.03	1.33
LSFO30	1.00	1.00	1.05	2.10
LSFO50	1.00	1.00	1.08	3.19

Appendix Table G2 Responses to various methane gas concentrations of un-doped and Sr(II) doped $LaFeO_3$ sensors operated at 400 °C

Perovskite sensor	Methane gas concentrations (ppm)				
	5000	10000	20000	30000	50000
LFO	1.06	1.23	1.56	1.50	1.16
LSFO10	1.06	1.15	1.34	1.26	1.09
LSFO30	1.28	1.58	2.10	1.92	1.38
LSFO50	1.71	2.40	3.20	2.85	1.40

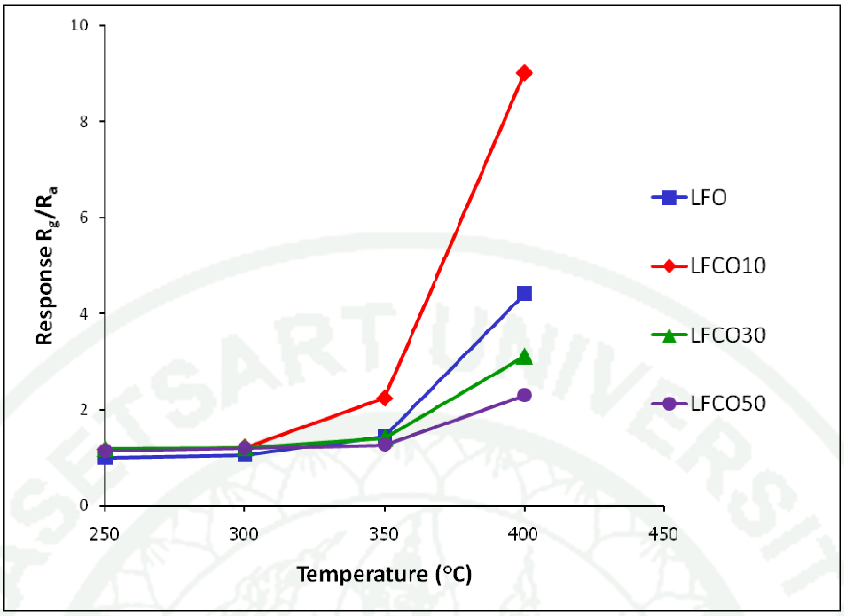

Appendix Figure G3 Responses to 50000 ppm methane gas of un-doped and Co(II) doped $LaFeO_3$ sensors operated at different temperatures.

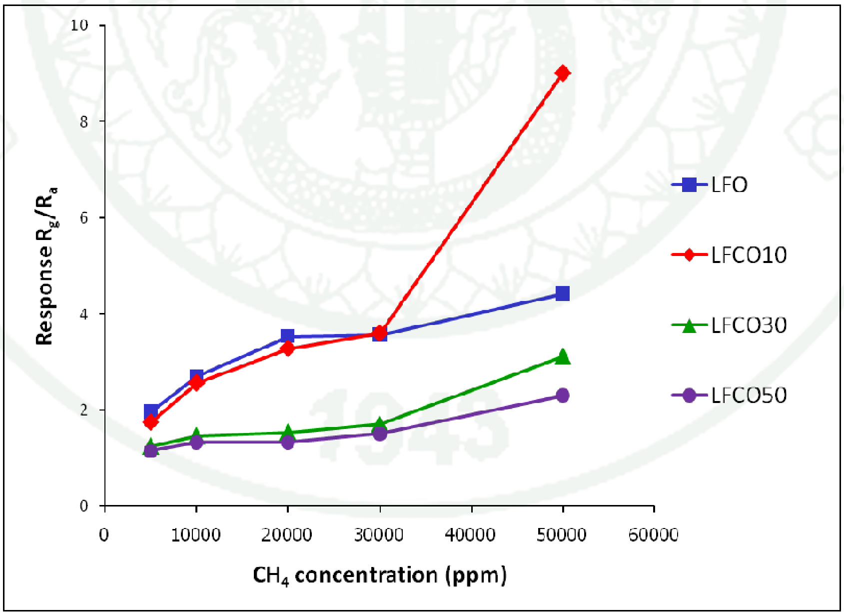

Appendix Figure G4 Responses to various methane gas concentrations of un-doped and Co(II) doped $LaFeO_3$ sensors operated at 400 °C.

Appendix Table G3 Responses to 50000 ppm methane gas of un-doped and Co(II) doped $LaFeO_3$ sensors operated at different temperatures

Perovskite sensor	Operating temperature (°C)			
	250	300	350	400
LFO	1.01	1.07	1.45	4.42
LFCO10	1.16	1.22	2.24	9.02
LFCO30	1.20	1.22	1.42	3.12
LFCO50	1.15	1.21	1.27	2.31

Appendix Table G4 Responses to various methane gas concentrations of un-doped and Co(II) doped $LaFeO_3$ sensors operated at 400 °C

Perovskite sensor	Methane gas concentrations (ppm)				
	5000	10000	20000	30000	50000
LFO	1.96	2.70	3.54	3.56	4.42
LFCO10	1.75	2.56	3.28	3.60	9.02
LFCO30	1.26	1.48	1.55	1.72	3.12
LFCO50	1.16	1.33	1.34	1.51	2.31

Appendix H

Hydrogen-sensing data of the un-doped, Sr(II) doped and Co(II) doped $LaFeO_3$

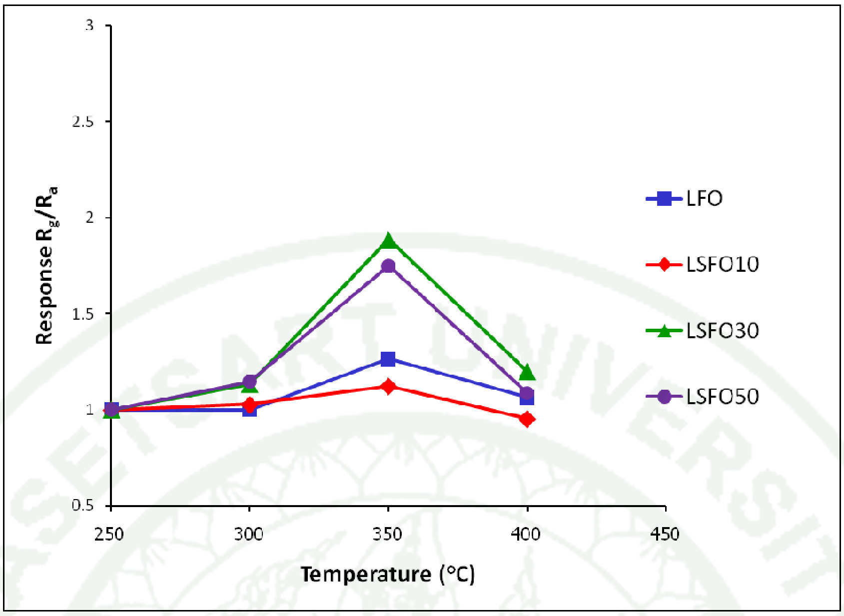

Appendix Figure H1 Responses to 30000 ppm hydrogen gas of un-doped and Sr(II) doped $LaFeO_3$ sensors operated at different temperatures.

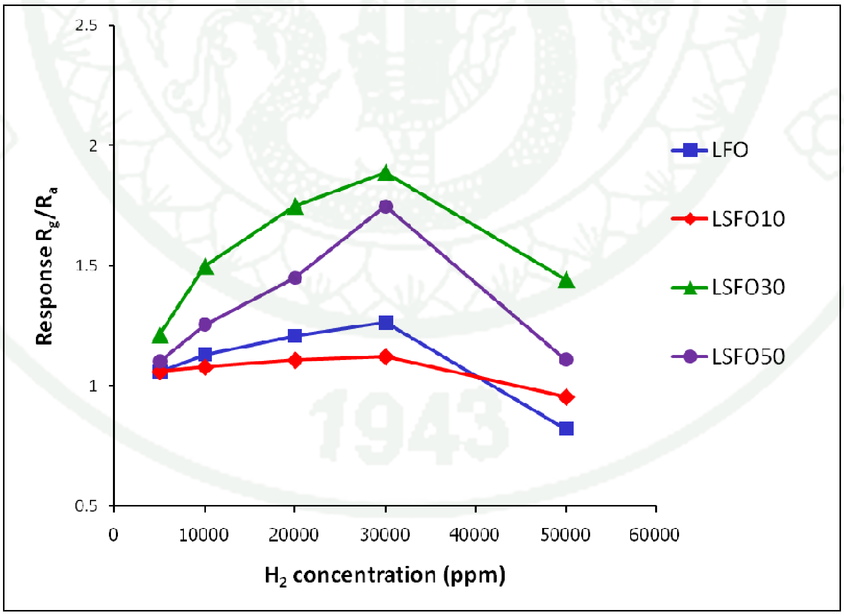

Appendix Figure H2 Responses to various hydrogen gas concentrations of un-doped and Sr(II) doped $LaFeO_3$ sensors operated at 400 °C.

Appendix Table H1 Responses to 30000 ppm hydrogen gas of un-doped and Sr(II) doped $LaFeO_3$ sensors operated at different temperatures

Perovskite	Operating temperature (°C)			
sensor	250	300	350	400
LFO	1.00	1.00	1.26	1.06
LSFO10	1.00	1.03	1.12	0.95
LSFO30	1.00	1.13	1.89	1.20
LSFO50	1.00	1.15	1.75	1.09

Appendix Table H2 Responses to various hydrogen gas concentrations of un-doped and Sr(II) doped $LaFeO_3$ sensors operated at 400 °C

Perovskite	Hydrogen gas concentrations (ppm)				
sensor	5000	10000	20000	30000	50000
LFO	1.06	1.13	1.21	1.26	0.82
LSFO10	1.06	1.08	1.11	1.12	0.96
LSFO30	1.21	1.50	1.75	1.89	1.44
LSFO50	1.10	1.26	1.45	1.75	1.11

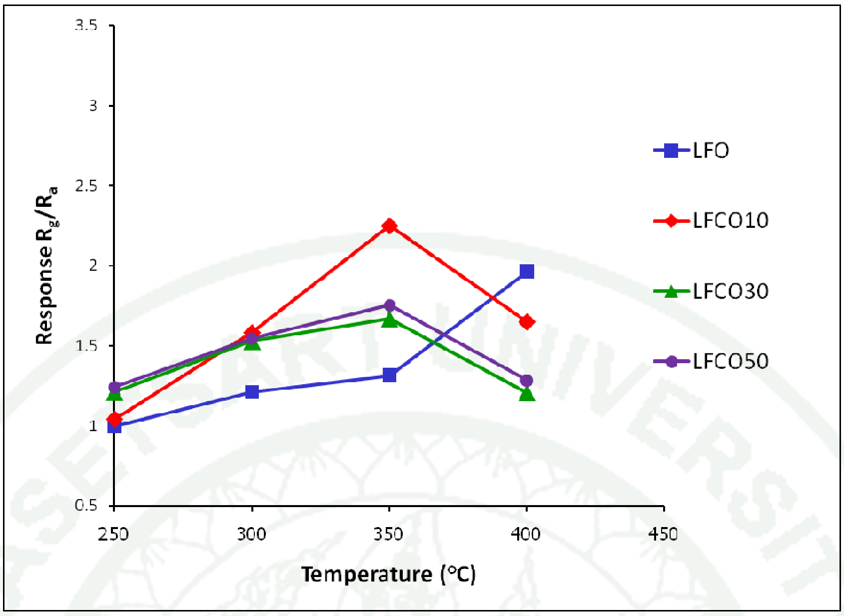

Appendix Figure H3 Responses to 30000 ppm hydrogen gas of un-doped and Co(II) doped $LaFeO_3$ sensors operated at different temperatures.

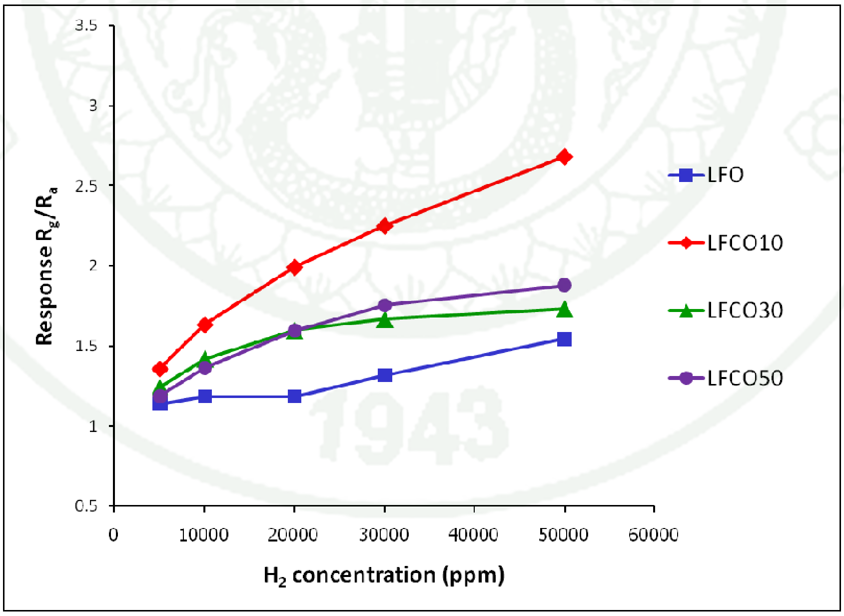

Appendix Figure H4 Responses to various hydrogen gas concentrations of un-doped and Co(II) doped $LaFeO_3$ sensors operated at 400 °C.

Appendix Table H3 Responses to 30000 ppm hydrogen gas of un-doped and Co(II) doped $LaFeO_3$ sensors operated at different temperatures

Perovskite	Operating temperature (°C)			
sensor	250	300	350	400
LFO	1.00	1.21	1.32	1.96
LFCO10	1.04	1.58	2.25	1.65
LFCO30	1.21	1.53	1.67	1.20
LFCO50	1.24	1.54	1.75	1.28

Appendix Table H4 Responses to various hydrogen gas concentrations of un-doped and Co(II) doped $LaFeO_3$ sensors operated at 400 °C

Perovskite	Hydrogen gas concentrations (ppm)				
sensor	5000	10000	20000	30000	50000
LFO	1.14	1.18	1.18	1.32	1.55
LFCO10	1.36	1.63	1.99	2.25	2.68
LFCO30	1.24	1.42	1.60	1.67	1.73
LFCO50	1.19	1.36	1.60	1.75	1.88

CIRRICULUM VITAE

NAME : Mr Thammanoon Thaweechai

BIRTH DATE : September 22, 1985

BIRTH PLACE : Chai Nat, Thailand

EDUCATION :

YEAR	INSTITUTE	DEGREE/DIPLOMA
2007	Kasetsart Univ.	B.Sc. (Chemistry)

POSITION/TITLE : Postgraduated student

WORKPLACE : Faculty of Science, Kasetsart University

SCHOLARSHIP/AWARDS : Thailand Graduate Institute of Science and Technology (TGIST), 2008